NASA TR R-437

RESULTS OF MAGNETOSPHERIC
BARIUM ION CLOUD EXPERIMENT OF 1971

David Adamson, Clifford L. Fricke,
and Sheila Ann T. Long

Langley Research Center
Hampton, Va. 23665

1. Report No. NASA TR R-437	2. Government Accession No.	3. Recipient's Catalog No.
4. Title and Subtitle RESULTS OF MAGNETOSPHERIC BARIUM ION CLOUD EXPERIMENT OF 1971		5. Report Date March 1975
		6. Performing Organization Code
7. Author(s) David Adamson, Clifford L. Fricke, and Sheila Ann T. Long		8. Performing Organization Report No. L-9914
9. Performing Organization Name and Address NASA Langley Research Center Hampton, Va. 23665		10. Work Unit No. 879-11-36-01
		11. Contract or Grant No.
12. Sponsoring Agency Name and Address National Aeronautics and Space Administration Washington, D.C. 20546		13. Type of Report and Period Covered Technical Report
		14. Sponsoring Agency Code

15. Supplementary Notes

16. Abstract

The NASA-Max Planck Institute Barium Ion Cloud (BIC) Experiment, performed on September 21, 1971, at 3:04:52 u.t., involved the release of about 2 kg of barium at an altitude of 31 482 km, a latitude of 6.926° N., and a longitude of 74.395° W. Significant erosion of plasma from the main ion core occurred during the initial phase of the ion-cloud expansion. From the motion of the outermost striational filaments, the electric-field components were determined to be 0.19 mV/m in the westerly direction and 0.68 mV/m in the inward direction. The differences between these components and those measured from balloons flown in the proximity of the extremity of the field line through the release point implied the existence of potential gradients along the magnetic field lines. The deceleration of the main core was greater than theoretically predicted. This was attributed to the formation of a polarization wake, resulting in an increase of the area of interaction and resistive dissipation at ionospheric levels. The actual orientation of the magnetic field line through the release point, as delineated by the ion cloud, differed by about 10.5° from that predicted by magnetic-field models that did not include the effect of ring current. There was no evidence of enhanced particle precipitation resulting from cloud deposition. An increase in the rate of elongation observed during the first 5 minutes may have resulted from a resonant cyclotron instability between the gyrating ions and extremely low frequency waves.

17. Key Words (Suggested by Author(s)) Plasma instabilities Magnetospheric physics Barium ion clouds	18. Distribution Statement Unclassified — Unlimited New Subject Category 46		
19. Security Classif. (of this report) Unclassified	20. Security Classif. (of this page) Unclassified	21. No. of Pages 62	22. Price* $4.25

CONTENTS

RESULTS OF MAGNETOSPHERIC BARIUM ION CLOUD

EXPERIMENT OF 1971

David Adamson, Clifford L. Fricke,
and Sheila Ann T. Long
Langley Research Center

SUMMARY

The NASA-Max Planck Institute Barium Ion Cloud (BIC) Experiment performed on September 21, 1971, at 3:04:52 u.t. involved the release of about 2 kg of barium at an altitude of 31 482 km, a latitude of 6.926^O N., and a longitude of 74.395^O W. The geomagnetic conditions were quiet. Significant erosion of plasma from the main ion core occurred during the initial phase of the ion-cloud expansion. The outermost striational filaments rapidly acquired the velocity of the ambient thermal plasma, thereafter drifting with an inward component of 0.995 km/sec and an easterly component of 3.62 km/sec (relative to an inertial frame). The corresponding electric field had components of 0.19 mV/m in the westerly direction and 0.68 mV/m in the inward direction. This differed considerably from the electric field measured from balloons flown in the proximity of the extremity of the field line through the release point, implying the existence of potential gradients along the magnetic field lines. The deceleration of the main core was greater than theoretically predicted. This was attributed to the formation of a polarization wake, resulting in an increase of the area of interaction and resistive dissipation at ionospheric levels. The actual orientation of the magnetic field line through the release point, as delineated by the ion cloud, differed by about 10.5^O from that predicted by magnetic-field models that did not include the effects of ring current. There was no evidence of enhanced particle precipitation resulting from cloud deposition. An increase in the rate of elongation observed during the first 5 minutes may have resulted from a resonant cyclotron instability between the gyrating ions and extremely low frequency (ELF) waves.

INTRODUCTION

During the past 15 years much has been learned about the distortions of Earth's magnetic field, caused by the impingement of the solar wind, by making magnetometer measurements from satellites and space probes. There remained, however, a scarcity of data on the configuration of the magnetospheric electric field. Some data pertaining to its azimuthal component had been obtained by determining the radial drift of whistler

ducts; however, such measurements are subject to quite large errors. Since it is generally believed that electric fields play an important role in fundamental dynamical processes (i.e., particle energization, precipitation, and diffusion), the importance of obtaining such data cannot be overstressed. In view of the successful use which had been made of barium-ion-cloud releases in the ionosphere for measuring ionospheric electric fields, NASA and the Max Planck Institute for Extraterrestrial Physics (MPE) jointly proposed, early in 1968, making a barium release within the magnetosphere. The technique developed by MPE is quite simple in principle. The barium, formed through a thermite-type reaction, is released as a neutral cloud and is rapidly ionized under solar irradiation. The ions, once formed, spiral along the magnetic field lines; and since they resonantly scatter in a visible wavelength (455.4 nm) of the solar spectrum, the ion cloud can be observed and photographed when viewed against a dark night-sky background. By assuming that the ion cloud, or a portion of it, acquires the motion of the ambient plasma, the electric-field vector can be determined from the magnetohydrodynamic (MHD) equation $\vec{E} + \vec{v} \times \vec{B} = 0$, where $\vec{v}$ is the velocity of the ion-cloud drift as established by the triangulation procedures and $\vec{B}$ is the magnetic induction. In addition to permitting a measurement of the electric field, the cloud effectively "paints" the magnetic field line over a substantial segment, approximately 15 000 km, providing an instantaneous delineation of its shape and orientation, something that is not possible from point measurements made by magnetometers. The ion-cloud technique is thus ideally suited for making deductions on magnetospheric-current flows.

The NASA-MPE Barium Ion Cloud (BIC) Experiment was performed on September 21, 1971, at 3:04:52 u.t. About 2 kg of barium were released at an altitude of 31 482 km (approximately 5 Earth radii), a latitude of 6.926° N., and a longitude of 74.395° W. The payload, designed and fabricated by MPE, was carried by a Scout vehicle launched by Wallops Flight Center from Wallops Island, Virginia, 3 hours 34 minutes earlier. The ion cloud that formed remained visible to the unaided eye for about 20 minutes and was tracked with cameras for about 1 hour 15 minutes.

This was the second experiment involving a release of barium in Earth's magnetosphere. In the earlier one, conducted by MPE (ref. 1), about 100g of barium were released at an altitude of about 11.5 Earth radii (about 75 000 km) from the European Space Research Organization Highly Eccentric Orbiting Satellite (HEOS I) on March 18, 1969. The cloud was tracked photographically for about 25 minutes. Even toward the end of this period, the velocity of the ion cloud deviated only slightly from that of the spacecraft and no determination of the electric field was possible.

In the BIC experiment, in addition to obtaining data on the electric field and magnetic-field-line shape and orientation, considerable information was obtained on interaction effects (e.g., on the formation of striations (ref. 2) and on the mechanism of

2

the momentum exchange with the ambient medium by which the cloud ultimately acquired the velocity of the ambient plasma).

A preliminary reporting of all pertinent scientific facets of the experiment was made at a special symposium on the NASA-MPE Barium Ion Cloud Experiment at the 53rd Annual Meeting of the American Geophysical Union in Washington, D.C. (ref. 3). The presentations of the U.S. participants were subsequently published on September 1, 1973, in the Journal of Geophysical Research (refs. 4 to 11).

This paper presents the complete results obtained from the BIC experiment. It represents an improvement in precision over preliminary results presented in an earlier paper (ref. 9). This improvement in accuracy has resulted from (a) refinements in triangulation data reduction procedures and (b) the inclusion of ring current. For completeness a brief discussion is included on striation formation although this topic has been treated in depth in reference 2. In addition, qualitative explanations are advanced for the first time for other interaction phenomena, such as energization, as evidenced by the increase in rate of elongation during the first 5 minutes, and the observed splitting of the main core and one of the striational filaments.

SYMBOLS

B magnetic field

E electric field

h altitude

I cloud brightness

I_0 maximum cloud brightness

j field-alined current

L geocentric distance of field-line/equatorial-plane intercept in R_E

ℓ length of cloud between half-brightness points

R_E Earth radii

t time

t_0	breakaway time (interval between striation formation and separation from main core)
v	velocity of ion-cloud drift
X_m, Y_m, Z_m	geomagnetic Cartesian axes
x_m, y_m, z_m	geomagnetic coordinates
Δv	velocity of striation relative to main core
τ	exponential deceleration time
$\rightarrow$	vector

SCIENTIFIC OBJECTIVES

General Considerations

The development of man's capability to make direct measurements in space using instrumented probes revised his concept of the geophysical environment. Up to 20 years ago it was generally believed that Earth's magnetic field was approximately that of a dipole, with its strength falling off as the inverse cube in all directions, as depicted in figure 1(a). It is now known that there is a continuous outstreaming of highly conducting plasma from the Sun which cannot penetrate Earth's magnetic field. This plasma, as it


(a) Pre-space-age.

(b) Present.
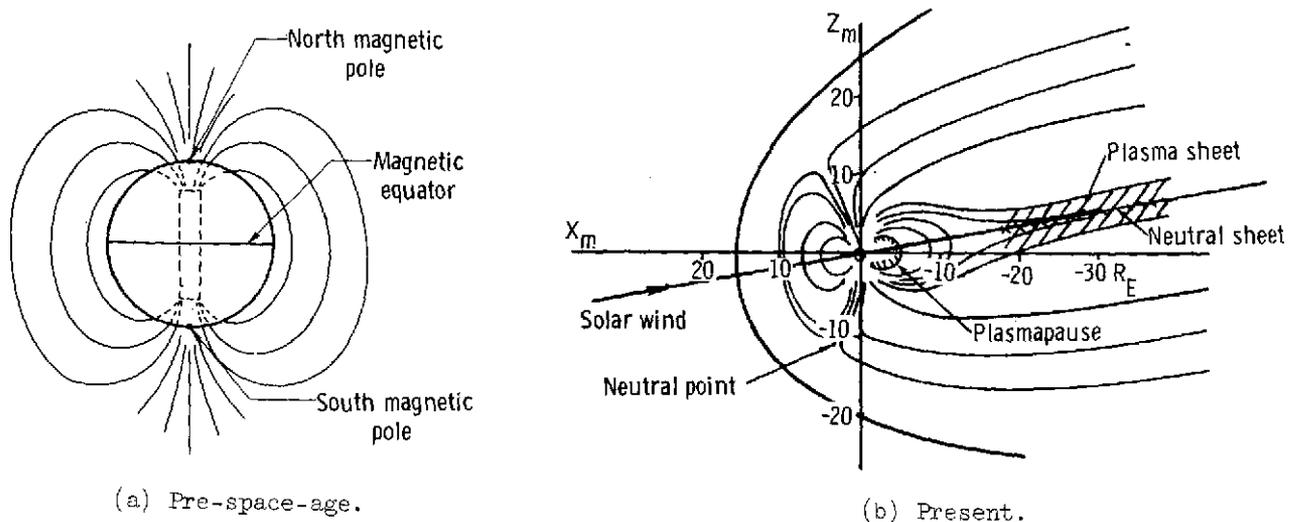
Figure 1.- Models of Earth's magnetic field.

impinges upon the magnetic field, compresses and flows around it and confines it — apart from some possible field-line merging — to the interior of the magnetospheric cavity. Magnetometers carried aboard satellites have provided much useful data bearing on the general topology of the magnetospheric magnetic field and this has led to the formulation of the model depicted in figure 1(b). Much data have also been obtained about the distribution of the energetic particles that populate the magnetosphere and their energy spectra. By contrast, much less is known about the magnetospheric electric field and the thermal particles whose motions are controlled by it. Some data have been obtained on the azimuthal component of the electric field by observing the radial drift of whistler ducts; however, such data are subject to large errors.

It should be stated at the outset that magnetospheric electric fields owe their origin to the existence of the insulating atmosphere. The solid Earth is itself a good conductor, and the bulk of the magnetosphere is an excellent conductor, having almost infinite conductivity along the magnetic field lines. Thus, if Earth's atmosphere were also conducting, there could be no charge accumulation and, therefore, no sustained motion of the magnetospheric plasma. Under these circumstances the imposition of stresses on the magnetospheric boundary would produce merely a distortion of the magnetic field. Stated another way, the field lines have identity within Earth's interior and throughout most of the magnetosphere, but within the atmosphere no such identity can be ascribed to them. As a consequence, the magnetospheric field lines can be interchanged with one another, the only energy needed being that expended in overcoming the frictional resistance at the ionospheric levels. The stresses which drive the convective motions are those associated with the streaming of the solar wind around the flanks of the magnetospheric boundary. Axford and Hines in reference 12 assume the stresses to be viscous in nature. On the other hand, Dungey, in reference 13 assumes that the stresses predominantly result from the merging of Earth's magnetic field lines with those of the interplanetary field entrained within the solar wind whenever the entrained field is oriented opposite to Earth's magnetic field. In the Dungey model the merging of the field lines is at the nose of the magnetospheric cavity. More recently it has been speculated by Frank (ref. 14) that field-line merging is limited to the polar cusp regions (clefts in the magnetic field down which plasma of the magnetosheath is continuously infiltrating). No matter what the nature of the stresses, the same kind of convective motion is induced — the plasma is dragged back along the flanks of the magnetopause and returns through the interior of the cavity. This convective motion is in fact not dissimilar to that within the cavity behind a blunt body moving through the air. If a magnetic tube in the geomagnetic tail is considered to be convected inward toward Earth, it will both shorten in length and diminish in cross section, thus compressing and energizing the entrained plasma. This is why the convective motions play an important role in the dynamical processes involving energization, particle precipitation, and plasma instabilities. Until these basic dynamical processes are better

understood, scientists cannot unravel such complex geophysical phenomena as geomagnetic storms, auroras, etc.

So far as the magnetic field is concerned, satellite magnetometer data are subject to the shortcoming that, since they consist of point measurements along the satellite trajectory, it is not possible to determine whether variations from one point to the next result from temporal variability or spatial inhomogeneities. In view of this it would seem highly desirable to supplement magnetometer data with an actual delineation of the field lines over a substantial fraction of their length through the use of barium ion clouds. The determination of shape and orientation of magnetic field lines would in turn provide valuable insights into the nature of the electric currents flowing within the magnetospheric cavity, especially the ring current.

It was with the purpose of providing such needed geophysical data on both electric fields and magnetic-field-line orientation that the BIC experiment was first proposed. These and some of the other objectives of the experiment are discussed below.

Objective 1: To Determine Magnitude and Direction of

Electric Field in Proximity of Release

The first scientific objective was to determine the magnitude and direction of Earth's electric field in the proximity of the barium release. At altitudes above 500 km, collisions are so infrequent that electrons can drift back and forth along magnetic field lines with almost infinite mobility. For this reason it is generally believed that the MHD approximation applies throughout most of the magnetosphere and that, therefore, the electric-field vector is directly related to the convective velocity of the thermal plasma through the expression $\vec{E} + \vec{v} \times \vec{B} = 0$. The barium ion cloud resonantly scatters sunlight in the visible portion of the spectrum and can therefore be seen when viewed against a dark night-sky background. Once the ion cloud has acquired the motion of the ambient thermal plasma, it is possible through triangulation to measure $\vec{v}$ and then through the aforementioned equation to calculate $\vec{E}$.

Objective 2: To Determine Shape and Orientation of

Magnetic Field Line as Delineated by Cloud

The second objective was to determine the shape and the orientation of the magnetic field line as delineated by the barium ion cloud. The barium ions, once they have formed, spiral up and down the magnetic field lines. The barium cloud thus effectively "paints" the field line that goes through the release point over a segment which is several Earth radii in length. The technique is thus ideally suited for comparing and evaluating magnetic-field models.

6

Objective 3: To Observe Transient Phenomena Associated With Release

The third objective was to observe the transient phenomena associated with the cloud release. If such a release is made in a relatively weak magnetic field the ions, as they are formed, will thrust the magnetic field lines apart, forming a diamagnetic bubble. The surface of this bubble is prone to various types of instabilities. Such instabilities might be expected to accelerate the process of the infiltration of field lines into the cloud interior. These transient phenomena are, of course, of interest in basic plasma physics. Moreover, they have interesting implications for geophysics, since the same phenomena might be expected to accompany the sudden intrusion of plasma into the inner magneto-sphere during geomagnetic storms.

Objective 4: To Observe Deceleration of Cloud

The fourth objective was to observe the cloud deceleration. The sudden injection of the ion cloud into the magnetic field results in a veering of the electrons to one side and the ions to the other. The resulting polarization field set up within the cloud interior permits the cloud to coast initially through the magnetic field with the velocity of the rocket from which the release was made. The subsequent mechanism of the momentum interchange between the cloud and the ambient medium, whereby the cloud ultimately acquires the velocity of the ambient plasma, is an interesting one in basic plasma physics. Moreover, since this mechanism involves field-alined currents between the cloud and the ionosphere and since there is now considerable evidence that many geophysical phenomena involve ionospheric-magnetospheric coupling through field-alined currents, this interaction is also one of considerable geophysical interest.

Objective 5: To Observe Additional Interaction Effects

The fifth objective was to observe additional interaction effects. If the deposition of the ion cloud results in a significant augmentation of the electron density, the presence of the cloud can result in an appreciable slowing down of the electron cyclotron waves propagating through the cloud interior. This might be expected to lead to increasingly strong interaction with the trapped-electron component leading to enhanced precipitation, thus promoting what might be described as an artificial aurora.

SELECTION OF RELEASE POINT

The release point was selected to optimize the achievement of the aforementioned scientific objectives. The requirements on the selection of the release point corresponding to the objectives, coupled with restraints imposed by range safety, resulted in a final

selection of the nominal release point at a latitude of 7.01° N., a longitude of 75.00° W., and 32 690-km latitude. These scientific requirements are discussed below.

Requirement 1: Measurement of Electric Field

The region in the proximity of the night-side equatorial plane at a geocentric distance between 6 and 7 Earth radii is of special geophysical interest. In this region the earthward (antisolar) convective flow external to the plasmapause encounters the plasma corotating with Earth within the interior of the plasmasphere. There has been speculation in the literature (ref. 15) that this region represents the site of the origin of the energetic particles that are associated with the nighttime auroras.

Requirement 2: Measurement of Magnetic Field

Magnetic-field models are now available that make allowance for the tilt of Earth's magnetic axis relative to the solar wind, the neutral sheet currents, and the magnetopause currents. At the present, however, there exists no theoretical model of the equatorial ring current that is generally valid. Such a ring current would be expected to produce the most marked perturbation to the magnetic field in the proximity of the magnetic equatorial plane. In order to examine best its effect on field-line shape, a release within 20° of the geomagnetic equator was required.

Requirement 3: Measurement of Transient Phenomena

If transient phenomena during the expansion of the cloud was to be observed, the release had to occur at a sufficiently high altitude so that the initial plasma pressure within the cloud was equal to or greater than the ambient magnetic-field pressure. This required that the release be above 25 000 km.

Requirement 4: Measurement of Deceleration of Cloud

A release at an altitude above 25 000 km ensured a sufficiently weak magnetic field so that the initial polarization electric field had a long persistence time and hence a correspondingly extended period of deceleration of the cloud. This permitted the details of the process to be more readily discerned than would be the case for a low-altitude release.

Requirement 5: Measurement of Additional Interaction Effects

Conditions conducive to particle precipitation resulting from cold-plasma injection required first that the volume into which the plasma was injected be outside the plasmapause to ensure a sufficiently low ambient electron density. In addition they required that

8

this volume be in the proximity of the equatorial plane where a sufficiently high density and anisotropy of the trapped electrons also contribute to strong particle-wave coupling.

Additional Considerations

Also, it was desirable to make the release on a field line having instrumented geophysical observatories at its extremities, in order to make correlative ground-based measurements at the time of the experiment on electric fields and other geophysical parameters of interest. Two conjugately placed stations ideally suited for this purpose were the Great Whale Geophysical Observatory in Quebec, Canada, and Byrd Station, Antarctica.

OBSERVATION SITES

Triangulation Sites

In reference 16 it has been shown analytically that, when triangulating from three observation sites on a point object in space, the highest precision is attained if the three sites together with the object are located very close to the apices of a regular tetrahedron. Because of the very high altitude of the BIC release, such a geometrical configuration was not possible. However, for selecting the triangulation sites the requirement was imposed that long baselines in both the north-south and the east-west directions be assured in the triangulation net.

An additional requirement was that the prime triangulation sites have a history of clear nighttime skies and stable weather characteristics that would permit a reliable prediction of photometric viewing for periods of at least 6 hours in duration. (It is recalled that 3 hr 34 min elapsed between the launch and the release.) Because of their geographic locations, climatological conditions during the launch-window periods for the experiment, and existing facilities, Mount Hopkins, Arizona, and Cerro Morado, Chile, were selected as two of the prime triangulation sites.

A site was needed on the east coast to satisfy the geometrical requirements; however, no such site could be found which also satisfied the weather requirements. Hence, it was decided to mount cameras on the NASA Convair 990, a high-altitude research aircraft, and to use it as an airborne observation platform flying out of NASA Wallops Flight Center. Unfortunately, at the time of the experiment the aircraft was grounded at Wallops due to an engine malfunction; nevertheless, clear skies permitted useful, though somewhat degraded, triangulation data to be obtained for the first hour.

Additional studies (refs. 17 and 18) confirmed that Mount Hopkins, Cerro Morado, and Wallops Island were so located, relative to each other and to the BIC release point,

△ Triangulation sites
▢ Additional optical sites
◯ Geophysical observatories
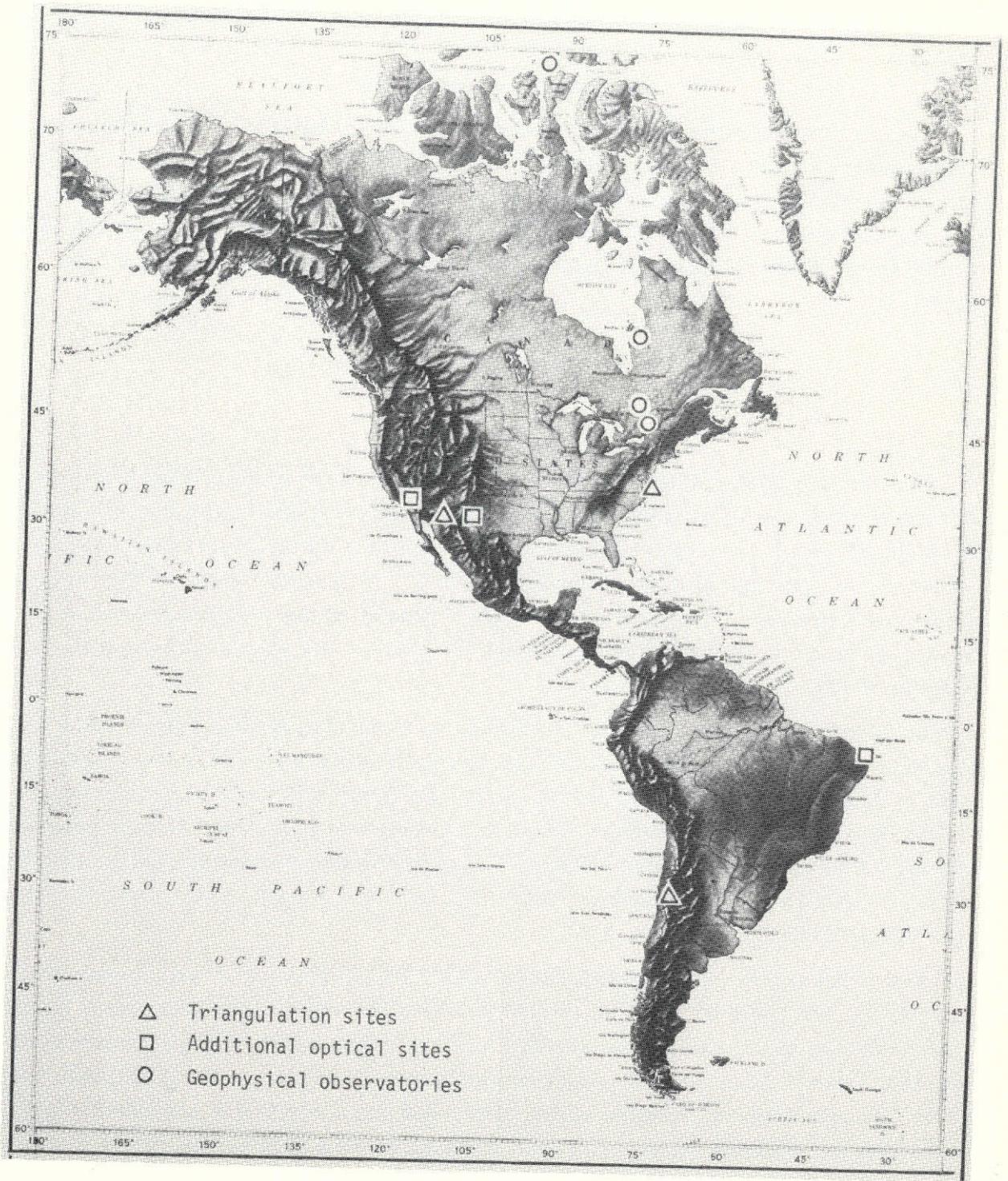
Figure 2.- The BIC observation sites.

as to give good triangulation results. Figure 2 shows the locations of these three triangulation sites. Their geographic coordinates are listed in table I.

The triangulation cameras were 70-mm format, 6-inch diameter, f/1 cameras, equipped with image intensifiers. They were all synchronized in time.

TABLE I.- GEOGRAPHIC COORDINATES OF BIC OPTICAL SITES

Site	Geographic lat., deg	W. long., deg	Altitude, km
Cerro Morado, Chile	-30.17	70.82	2.19
Edwards Air Force Base, California	34.96	117.91	.08
Mount Hopkins, Arizona	31.69	110.88	2.36
Natal, Brazil	-5.93	35.16	.04
Wallops Flight Center, Virginia	37.93	75.47	.01
White Sands, New Mexico	32.42	106.55	1.65

Additional Optical Sites

Baker-Nunn cameras of the Smithsonian Astrophysical Observatory (SAO) were located at Edwards Air Force Base, California; Natal, Brazil; and at Mount Hopkins, Arizona. These three Baker-Nunn cameras plus a Langley Research Center 36-inch, f/3 telescope and some additional electronic imaging systems at White Sands, New Mexico, were used to obtain high resolution optical data. The locations of these additional optical sites are shown on the map in figure 2 and their geographic coordinates are listed in table I.

Geophysical Observatories

Geophysical observatories were included to obtain data on the geophysical conditions during the experiment and to monitor any induced changes that might occur. The observatory at Great Whale, Quebec, located close to the foot of the geomagnetic field line on which the neutral barium was released, was equipped with magnetometers, auroral all-sky cameras, auroral photometers, high-frequency auroral radar, an ionosonde, 30- and 38-MHz riometers, and whistler receivers. Magnetometers were also located at Ottawa, Ontario, and at Resolute, Cornwallis Island, Canada. Whistler receivers were also located at Byrd Station, Antarctica, and at Roberval, Quebec. The locations of these geophysical observatories, except Byrd Station, are shown on the map in figure 2. The geographic coordinates and the types of measuring devices at each of them are listed in table II.

TABLE II.- GEOGRAPHIC COORDINATES AND MEASURING DEVICES OF BIC GEOPHYSICAL OBSERVATORIES

Site	Geographic lat., deg	W. long., deg	Measuring devices
Byrd Station, Antarctica	-79.98	120.02	Whistler receivers
Great Whale, Quebec	55.30	77.75	Magnetometers Auroral all-sky cameras Auroral photometers High-frequency auroral radar Ionosonde 30- and 38-MHz riometers Whistler receivers
Ottowa, Ontario	46.00	76.00	Magnetometer
Resolute, Cornwallis Island	74.50	95.00	Magnetometer
Roberval, Quebec	48.00	72.00	Whistler receiver

In addition, two balloons were launched from Great Whale about an hour prior to the experiment. These carried X-ray monitors and instruments to measure ionospheric electric fields.

QUALITATIVE DISCUSSION OF CLOUD EVOLUTION

General Description

In order to facilitate the discussion of the results obtained, it is desirable first to orient the reader by providing a brief qualitative description of the cloud evolution. The release was made on September 21, 1971, at 3:04:52 u.t. (corresponding approximately to 22:30 magnetic local time) at an L of approximately 7.1 and a magnetic latitude of 18.4^O N. as shown in figure 3. (The geomagnetic and B-L coordinate systems are defined in ref. 19, pp. 8-9.)

The photograph in figure 4(a) was taken at 3:06:26 u.t. with the Langley Research Center 36-inch, f/3 telescope, equipped with an image intensifier, located at White Sands, New Mexico. The spherical neutral cloud consisted of strontium, present in the payload as an impurity, and a small amount of barium that was not yet ionized at the time the photograph was taken. The bright bar through the center is the main core of the ionized cloud and is alined with the magnetic field. It is noted that field-alined striational features exist on both sides of the main core. These consist of plasma eroded from the
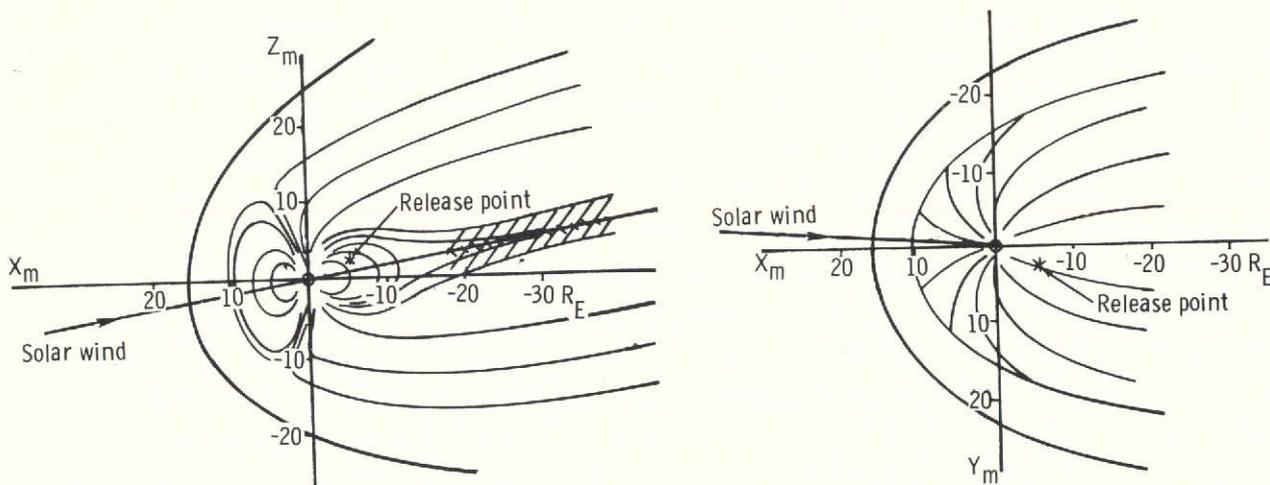
Figure 3.- Ion-cloud release location (referred to geomagnetic coordinate frame).
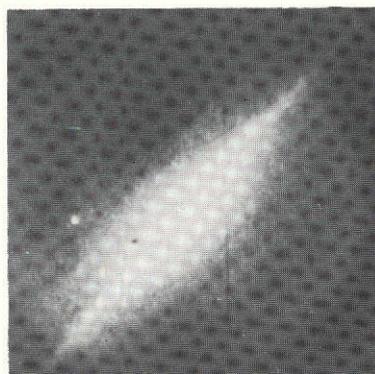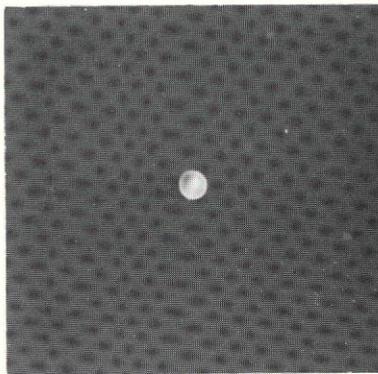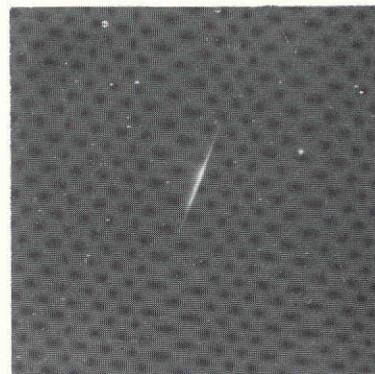
(a)   3:06:26 u.t.   (b)   3:07:03 u.t.   (c)   3:09:49 u.t.
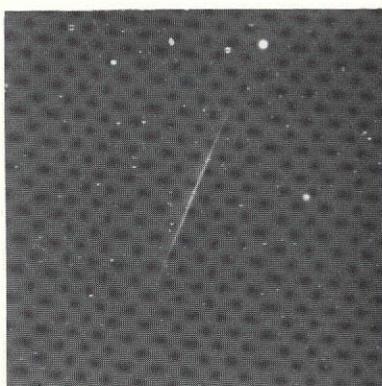
(d)   3:13:52 u.t.   (e)   3:16:37 u.t.
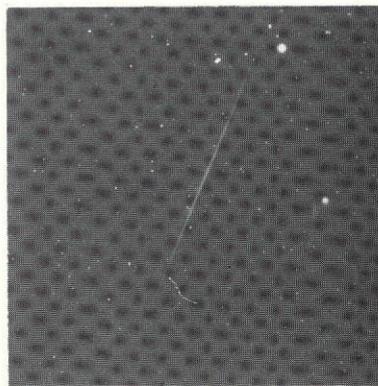
Figure 4.- Photographs of barium cloud at early times from White Sands
(fig. 4(a) only) and Mount Hopkins.

main core during the transient phase of the cloud expansion, as discussed in reference 2.
The next sequence of four photographs in figures 4(b) to (e) was taken with the Baker-
Nunn camera located at Mount Hopkins, Arizona. It is noted from figure 4(b), taken at
3:07:03 u.t., that the image of the neutral cloud exhibits a pronounced ring structure.
This is characteristic of neutral-gas releases in the extreme vacuum of space existing at
altitudes above 500 km. Thus, at the termination of the collision-dominated phase of the
expansion, which lasts only a second or two, the velocity spread of the particles is quite
small in comparison with their mean radial velocity. The neutral particles, thereafter,
remain confined within a rather thin spherical shell. This phenomenon is discussed in
reference 20. From the vantage point of Mount Hopkins, the ion cloud is drifting from
left to right. It is noted that the leading edge of the ion cloud in figures 4(c) to (e) is quite
sharp. All of the eroded plasma has apparently fallen behind into the wake of the main
core. This is especially evident in the sequence of photographs in figures 5(a) to (d)
taken with the high-gain image-intensifier camera system specially designed for this
experiment. It is noted that the spherical neutral cloud is still clearly discernible in
figure 5(a) taken at 3:20:20 u.t. The fact that the neutral cloud, which consists of 10g to
20g of strontium, is about 2000 km in diameter at this time is convincing testimony of the
sensitivity of the instrument. It is also noted from this figure that the ion cloud, even
after the lapse of 15 minutes, remains approximately centered on the neutral cloud, which
of course continues to move with the velocity of the rocket. This motion of the ion cloud
is related to the acquisition of polarization charges on the lateral faces of the cloud, as
discussed in the subsection entitled "Theory of Deceleration of Ion Cloud." Attention is
drawn in figure 5(b), corresponding to the epoch 3:25:00 u.t., to the six equispaced stri-
ations lying close to the main core. The main core, by virtue of its relatively high density
and momentum, continues to move for an extended period with a velocity almost equal to
that of the spacecraft. Less obvious are the mechanisms which allow these tenuous stri-
ational features to keep pace with the main core. There are sound reasons for believing
that these striational features were entrained within a polarization wake existing behind
the main core, as discussed in the subsection entitled "Implications for Existence of
Polarization Wake." By 3:30:00 u.t. (fig. 5(c)), the striations have faded markedly, except
the one closest to the main core. It remains clearly visible at 3:39:30 (fig. 5(e)) and is
barely discernible at 3:45:00 u.t. (fig. 5(f)). Thereafter, only the main core can be
observed (figs. 5(g) and (h)).

Formation of Striations

The nature of the instability leading to the formation of the striations is discussed
at length in reference 2. The arguments developed there support the contention that the
striations result from a Rayleigh-Taylor instability operative at the ion-cloud boundary
during the transient phase of the ion-cloud expansion. Thus, whereas the elongation of

14
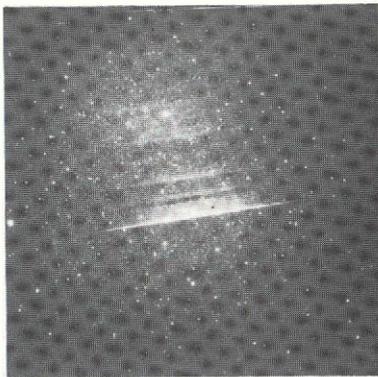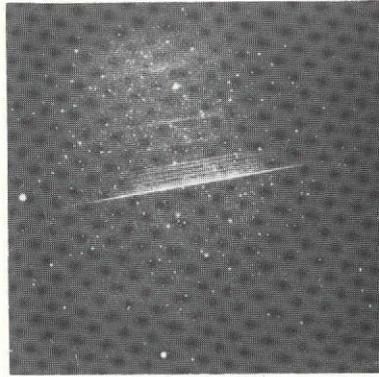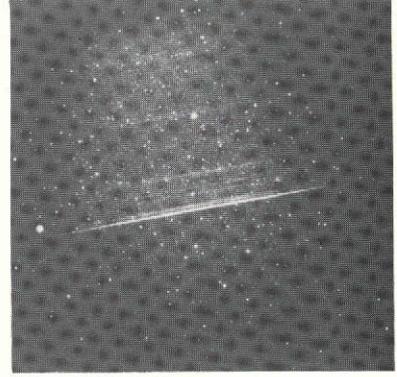
(a) 3:20:20 u.t.   (b) 3:25:00 u.t.   (c) 3:30:00 u.t.
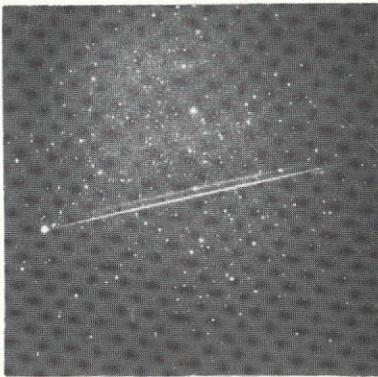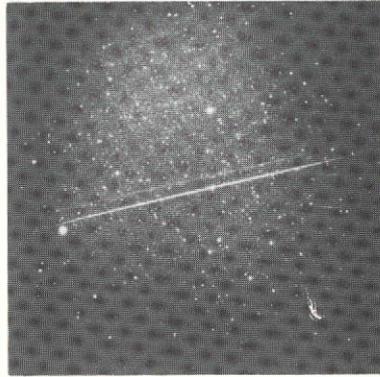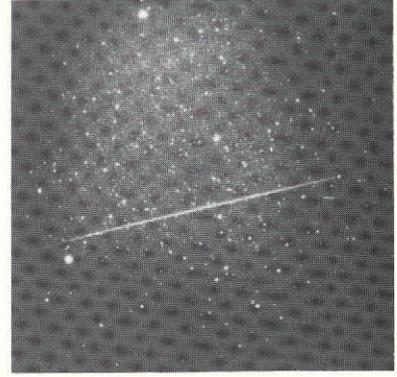
(d) 3:35:10 u.t.   (e) 3:39:30 u.t.   (f) 3:45:00 u.t.
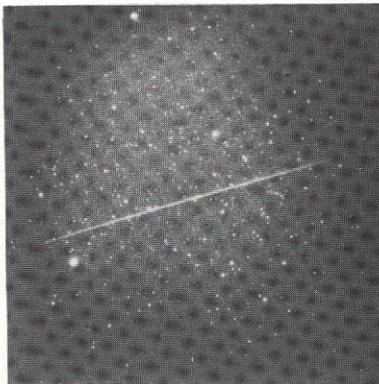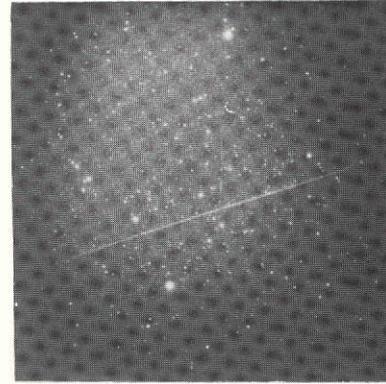
(g) 3:49:00 u.t.   (h) 4:00:30 u.t.

L-75-138

Figure 5.- Photographs of barium cloud from Cerro Morado at
early and intermediate times.

15
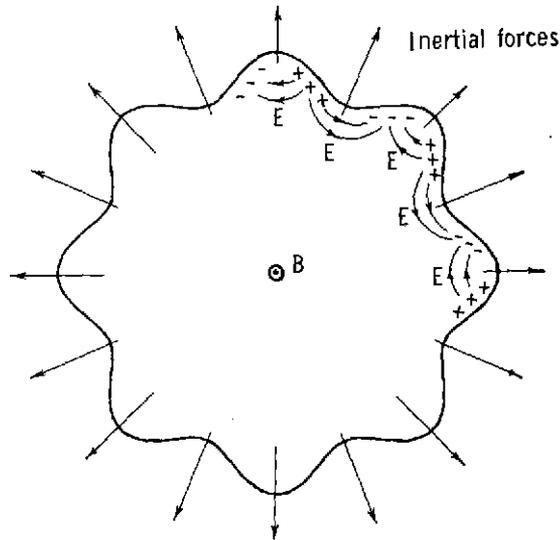
Figure 6.- Rayleigh-Taylor instability at boundary of expanding ion cloud.

the cloud in the direction of the magnetic field proceeds without impediment, its transverse expansion is opposed by an inwardly directed magnetic pressure. During the resulting radial deceleration the inertial forces acting on the plasma are radially outward. The situation is depicted in figure 6. If the magnetic field is out of the plane of the paper, the radially outward force induces an ion drift in the clockwise direction and an electron drift in the counterclockwise direction. If the boundary is assumed to be rippled, the accumulation of charges and the associated electric field within the plasma are as shown. Clearly the polarization electric field causes the plasma to drift with a radial velocity $\dfrac{\vec{E} \times \vec{B}}{B^2}$, accentuating the undulation at the boundary. This growing instability eventually leads to the detachment of the plasma around the entire boundary and explains the presence of the striated plasma on both sides of the core, as observed in the photograph taken shortly after the release (fig. 4(a)).

Splitting of Ion Cloud

Another interaction phenomenon of interest is evidenced by the splitting of the main core and one striational filament, as shown in figures 7(a) to (d). Figures 7(c) and (d) show the splitting of the main core, indicated by the arrows, at very late times. As the main core moves through the ambient medium, ions are shed from one side and electrons from the other; indeed, it is this shedding of charged particles of opposite sign that gives rise to the polarization wake to which reference has already been made. The shedding of charge is accompanied by a drifting of ions from one side to the other through the cloud interior and a progressive building up of ion-density differential across the cloud diameter. This, in turn, leads to a shearing action across the cloud, the less-dense portion being

16
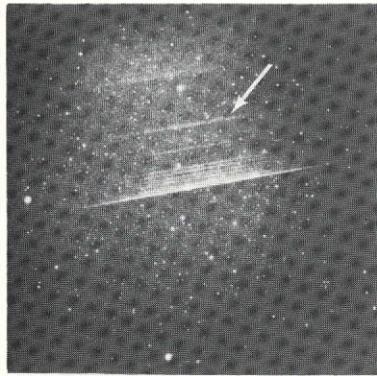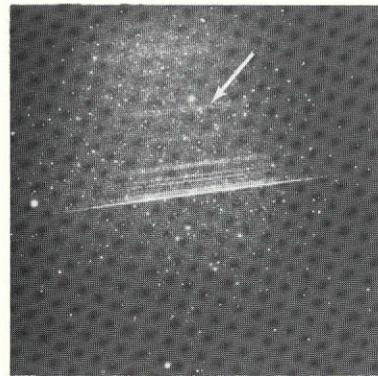
(a) 3:24:30 u.t.   (b) 3:28:10 u.t.
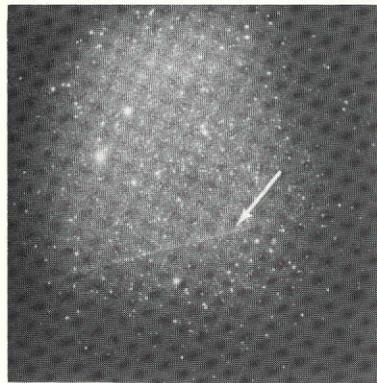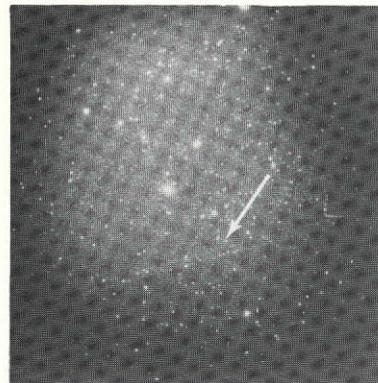
(c) 4:14:10 u.t.   (d) 4:18:20 u.t.

L-75-139

Figure 7.- Photographs of barium cloud from Cerro Morado showing
splitting of one of the striations, (a) and (b), and splitting
of main core, (c) and (d).

subject to the greater deceleration. The shearing action and the associated distortion of the cloud cross section lead eventually to a pinching down and splitting of the cloud along its length. Thereafter, the two portions separate quite rapidly. The same phenomenon was also observed in the case of one of the more prominent striational features (figs. 7(a) and (b)).

GROWTH OF MAIN CORE

Densitometric Analysis

The photographs for the densitometric analysis were those taken with the Baker-Nunn camera located at Mount Hopkins, Arizona. These were chosen in preference to those taken with the triangulation cameras which used image intensifier systems because of their reduced graininess.
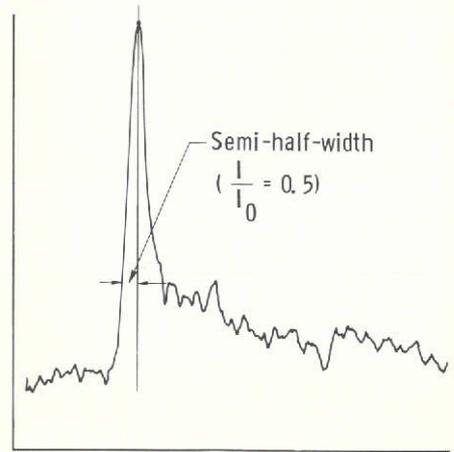
(b) Microdensitometer trace along a-a.

L-75-140
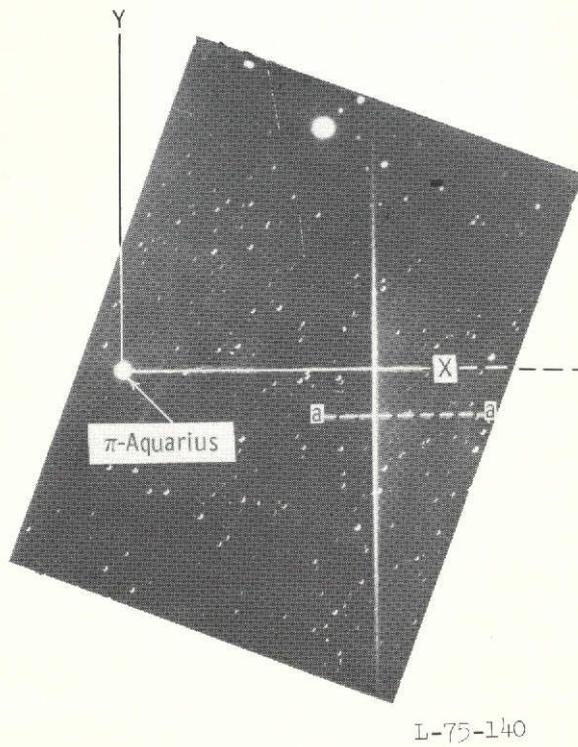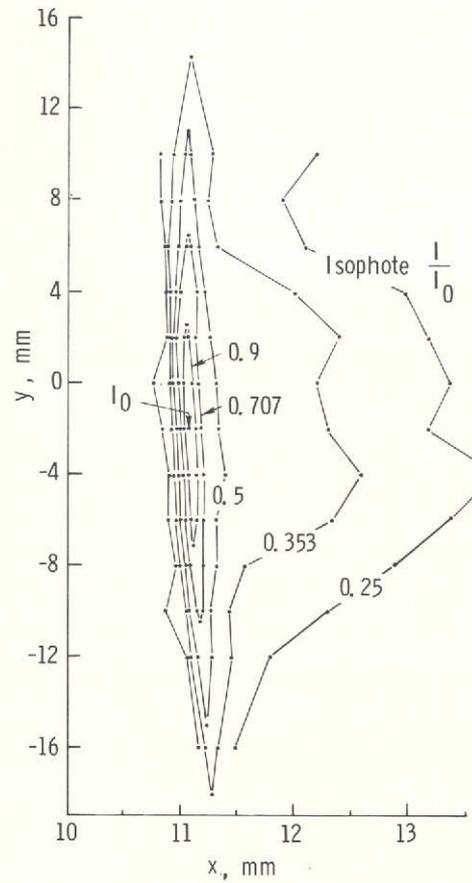
(a) Photograph.

(c) Isophote contours.

Figure 8.- Densitometric analysis of photograph taken at 3:16:05 u.t.

A frame chosen for analysis was placed on the specimen table of a scanning micro-densitometer and oriented such that the cloud filament was perpendicular to the direction of traverse (fig. 8(a)). A datum traverse was then run through the center of some pre-selected star (π-Aquarius, in the present instance). Further traces were made on either side of the datum over the entire observable length of the cloud image. In addition, a scan was made along the film sensitometric strip to establish the relation between the microdensitometer deflection and the brightness. Edward R. Manring and Richard R. Patty of North Carolina State University assisted in this phase of the analysis.

Cloud Width as Function of Time

Some care has to be exercised in defining cloud width. Thus, in the sample micro-densitometer trace shown in figure 8(b), the profile is noticeably asymmetric as a consequence of the existence of striated plasma on the downwind side of the cloud. The semi-half-width of the main core has been defined as the distance from the vertical line drawn through the profile peak to the half-brightness point on the upwind portion of the profile. The entire half-width at the median section is presented as a function of time in figure 9(a).
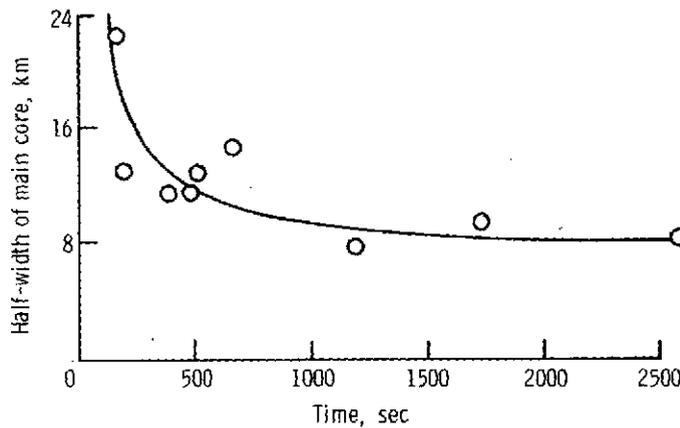
(a) Width as a function of time.

Figure 9.- Growth of main core.

Cloud Length as Function of Time

The cloud length, defined as the actual spatial separation between the half-brightness points, was obtained in the following manner. From the several microdensitometer traces taken along the cloud length, a contour plot was prepared as shown in figure 8(c). From the isophote corresponding to half of the peak brightness, the x- and y-coordinates of the half-brightness points on the cloud centerline were determined, thus defining two lines of sight in space through the observation site. The final step consisted in locating those points on the main core (determined from multistation-triangulation data) lying closest to
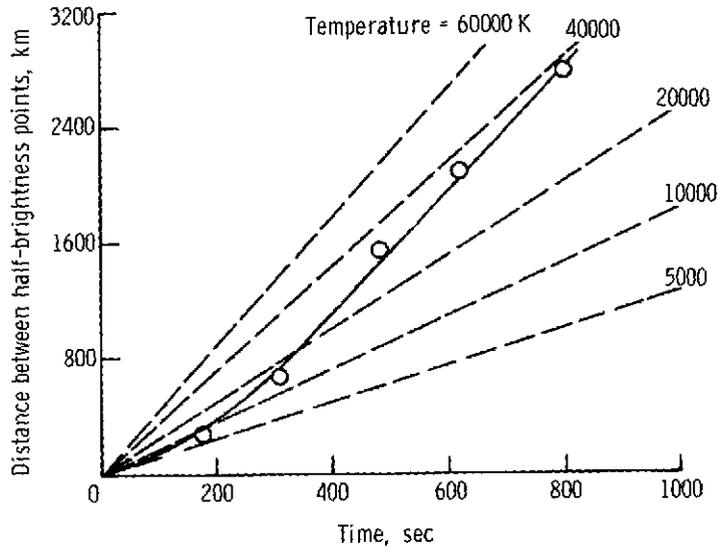
(b) Length as a function of time.

Figure 9.- Concluded.

the lines in question. The cloud length is given as a function of time by the solid curve in figure 9(b).

In appendix A of reference 9 the following expression is obtained for the length ℓ of the ion cloud between the half-brightness points as a function of the temperature and the time, by assuming that the ions are injected into the magnetic field with a Maxwellian velocity distribution:

$$\ell = (8 \ln 2)^{1/2}\left(\frac{kT}{m_{Ba}}\right)^{1/2} t$$

where k is the Boltzmann constant, T is the temperature, m_{Ba} is the mass of a barium ion, and t is the time.

By using this expression, curves corresponding to the temperatures of 5000, 10 000, 20 000, 40 000, and 60 000 K were calculated (see dotted curves in fig. 9(b)). It is noted that the initial rate of elongation of the main core corresponds to a temperature of about 4000 K which, considering the reaction temperature and the likelihood of some energization through photoionization, is perhaps what might have been expected. Since the ion-ion collisions become negligible within several seconds and the photoionization is essentially completed within 30 seconds, the continuing buildup of the rate of elongation over a period of 5 minutes indicates a significant energization of the ions (i.e., up to a temperature of about 60 000 K) resulting from an interaction with the ambient medium. This is discussed further in the subsection entitled "Interaction Effects."

20

Cloud Density as Function of Time

By using contour plots of selected Baker-Nunn photographs (similar to fig. 8(c)), in conjunction with photometric data of the release (ref. 7), quantitative estimates of the ion distribution within the main core were made. A plot of the ion density at the center of the main core is given as a function of time in figure 10. At 100 seconds the peak ion density is about 4×10^{10} m^{-3} and the temperature (from fig. 9) is about 20 000 K. If it is further assumed that the magnetic-field strength in the proximity of the release is 188 gammas, then the value for β (i.e., the ratio of plasma kinetic pressure to magnetic-field pressure) is approximately unity.
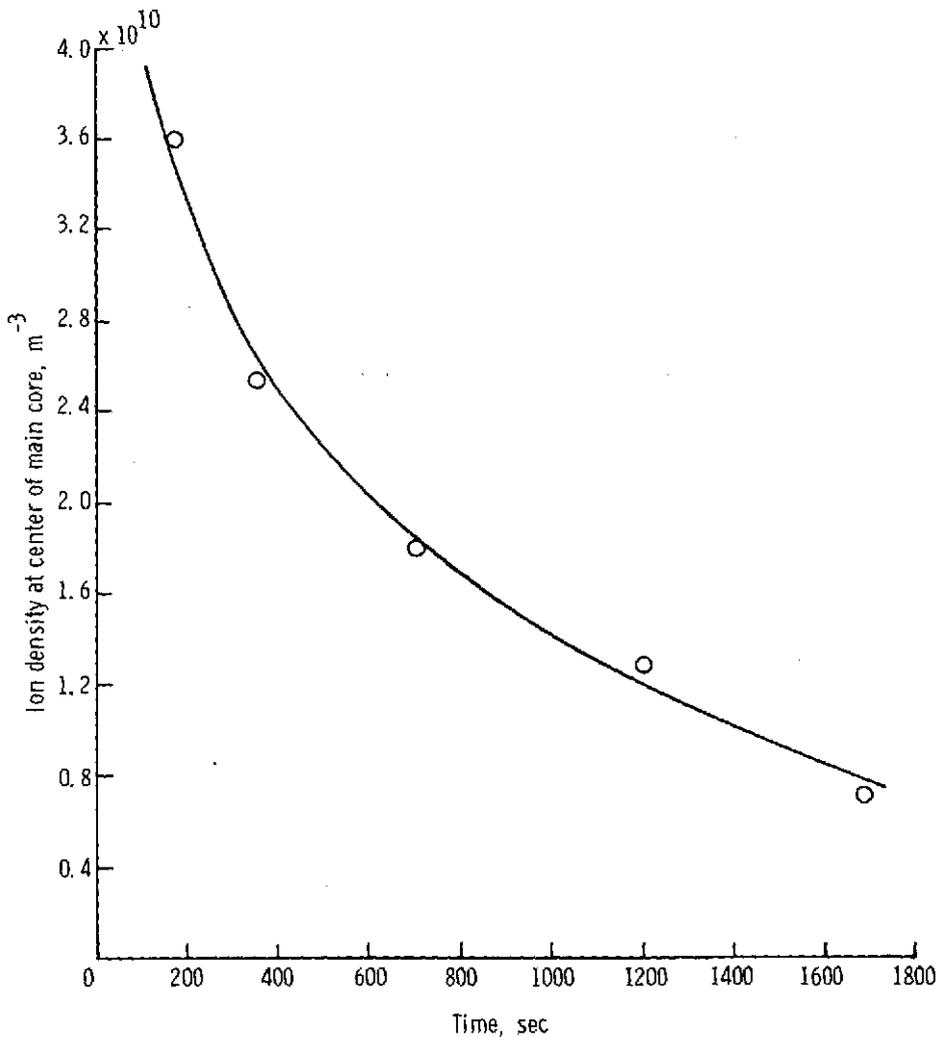
Figure 10.- Peak ion density in main core as a function of time.

DATA REDUCTION AND TRIANGULATION

The accuracy of locating the cloud by triangulation methods was limited because the baselines available were relatively short compared to the high altitude of the release. This is illustrated in figure 11. Hence, it was necessary to use every means possible to improve the accuracy by calibrating for the distortion in the cameras, by precisely determining the orientation of the cameras by means of stars in the photographs, and by using data from three triangulation sites.

The data reduction can be broken down into the following steps:

(1) The measurement of several hundred stars on one calibration frame in order to correct for distortions in the image intensifier and lens systems.

(2) The measurement of the x- and y-coordinates of a few hundred points along the centerline of the cloud on each data frame, along with the measurement of the coordinates of most of the star images on each frame to be used for the camera orientation.

(3) The conversion of the x- and y-coordinates of the cloud image into azimuth-elevation coordinates from each triangulation site using a computer program.

(4) The triangulation of the azimuth-elevation data from all of the sites at a given time using a computer program, which gives the latitude and longitude of the cloud center-line as a function of altitude.

(5) The smoothing and plotting of all of the data to obtain the cloud coordinates as a function of time.

Step 1: Calibration of Image Intensifier

The use of electronically enhanced images was required because of the faintness of the cloud (resulting from the cloud's low density) and the need for short exposures to avoid image smearing. Unfortunately, the distortion caused by the intensifier gave an rms error on the order of 0.1^O of arc if no corrections were made. This error is about 20 times that for a good lens system without an intensifier. The method of calibration used (ref. 21) reduces the rms error to 0.0025^O of arc.

The x- and y-coordinates of 300 to 400 star images on one calibration frame are measured using a comparator in conjunction with an automatic card punch. Once all the stars are identified, a calibration computer program that makes use of a built-in star catalog computes the corrections needed to convert the image coordinates to the true position of the stars. A seventh-order-polynomial correction is then found by a least-squares curve fitting. This seventh-order correction can then be used to correct all images on subsequent data frames.
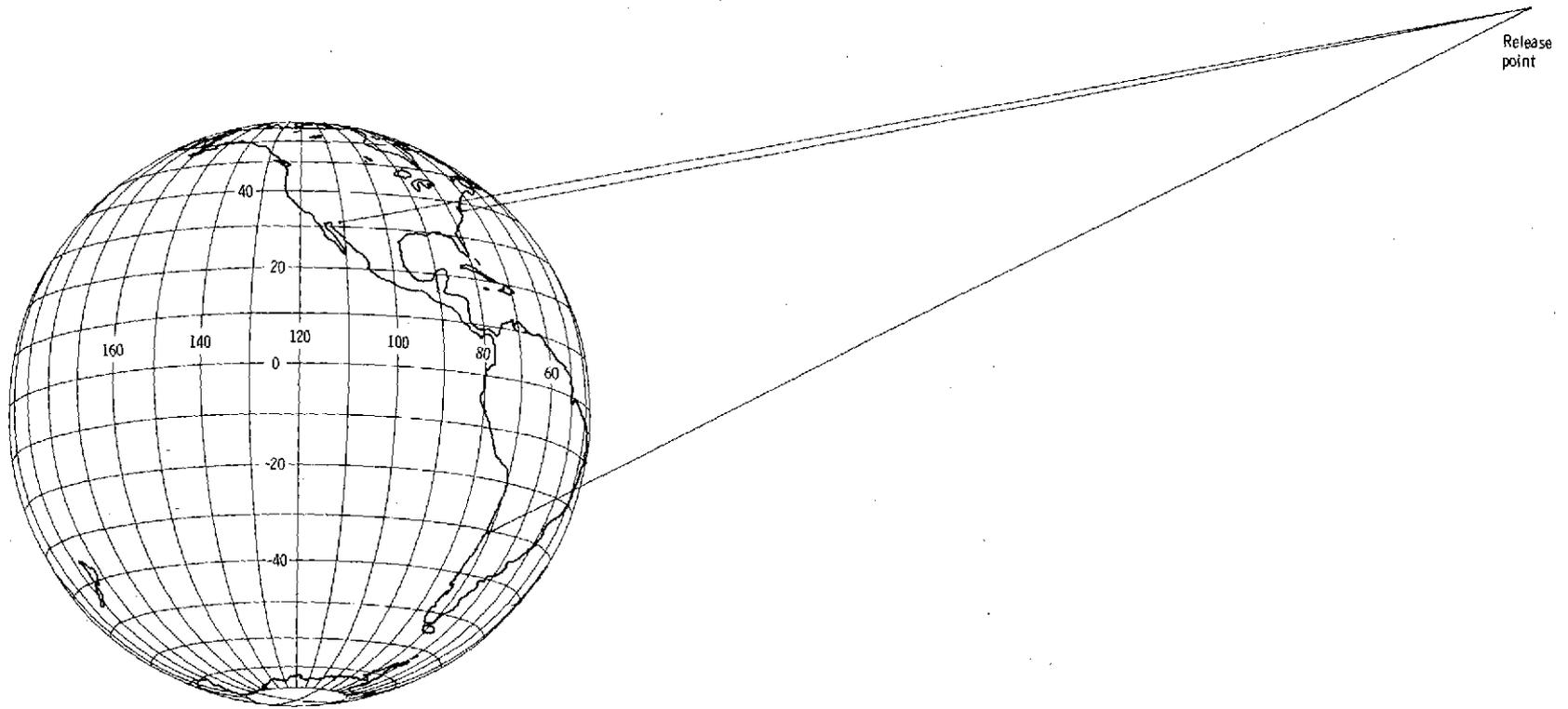
Figure 11.- Lines of sight from triangulation sites to BIC release point.

The computer program can be used to help identify the stars on the calibration frame. Once several of the stars have been identified manually, a preliminary correction can be made so that the program can then identify the remaining stars.

Step 2: Measurements on Data Frame

One of the major sources of error occurs because of the finite width of the cloud image, which is on the order of 0.015^o of arc. During late times, the image is much wider and less distinct. In order to define the centerline as accurately as possible, a large number of measurements was made (as many as 100 to 200) along the length of the cloud image, thus permitting statistical averaging.

In order to determine the camera orientation of the data frame, the coordinates of several (15 or more) star images are measured. Four to eight of these stars must be identified.

Step 3: Conversion of Cloud Image Points to Azimuth and Elevation

All the data points and star points on the data frame are corrected for distortion using the results from the camera calibration. The identified stars are used for a preliminary orientation of the data frame so that the other stars can be automatically identified using a computer program. Then, all the stars are used in the computer program, which makes a least-squares fit to all the stars (refs. 22 and 23) to find the precise camera orientation. Thus, the precise direction of each datum point can be determined.

The program then converts the x- and y-coordinates to right ascension-declination coordinates. Subsequently, it calculates the azimuth-elevation coordinates using the observation-site coordinates and the time of the data frame.

Step 4: Triangulation

The azimuth-elevation data from one observation site define a conical surface in space. Similar data from another site define another conical surface. Thus, the intersection of these two surfaces uniquely determines a curved line in space. When more than two sites are used and errors occur in the lines of sight, the intersection is not unique and some method of averaging must be used. Reference 24 describes a computer program that accomplishes this by finding solution points along the line in space which minimize the rms of the residuals from each site. The residual from a given site is defined as the angle between the line of sight to a trial solution point and the conical surface defined by the azimuth-elevation curve from that site. One important feature of the program is that the computation of the residuals uses a least-squares smoothed curve fit to the azimuth-elevation data points in the vicinity of the trial solution. The output of the computer program is the latitude and longitude as a function of altitude for each time.

24

Step 5: Smoothing and Plotting of Data

The output of the triangulation program can be assembled in the form of latitude and longitude as a function of time at various altitudes. In this form the latitude and the longitude are each considered as polynomial functions of the two independent variables time and altitude in order to find a least-squares fit to all the data. A computer program accomplishes this and plots the results.

The triangulation data reduction on the BIC experiment was the joint effort of the authors and W. F. Landon and D. L. Ridge of Wallops Flight Center.

DELINEATION OF MAGNETIC FIELD LINE BY MAIN CORE

Triangulation of Main-Core Data

Release point.- The release point was determined from the triangulation of the cloud when it first appeared as a point and also from telemetry and radar trajectory data. The results are (release time is 3:04:52 u.t.) shown in table III.

TABLE III.- RELEASE POINT DETERMINED FROM
TRIANGULATION AND RADAR

	Triangulation release point	Radar release point
Latitude	6.926^O	6.968^O
Longitude	74.395^O W.	74.403^O W.
Altitude	31 482 km	31 482 km

Expressed in geomagnetic Cartesian coordinates the triangulated release point corresponds to $x_m = -32\ 064$ km, $y_m = 16\ 290$ km, and $z_m = 11\ 818$ km. In this coordinate system z_m is alined with the magnetic dipole axis and directed toward north; X_m lies in the plane containing the dipole axis and the Earth-Sun line is perpendicular to the dipole axis, and points in the general direction of the Sun; and Y_m completes the right-handed triad.

Latitude.- Figure 12 shows the latitude as a function of time of each triangulated point on the main cloud for altitude levels spaced 500 km apart. The solid lines show the least-squares fit, where 20 points with deviations greater than 0.3^O were discarded and 594 points were kept. The function is given in degrees by

$$Latitude = 24.8465 + 0.00015394h + 0.14978t - 2.2695 \times 10^{-8}h^2 - 0.00023665t^2$$

$$- 6.11654 \times 10^{-6}ht$$
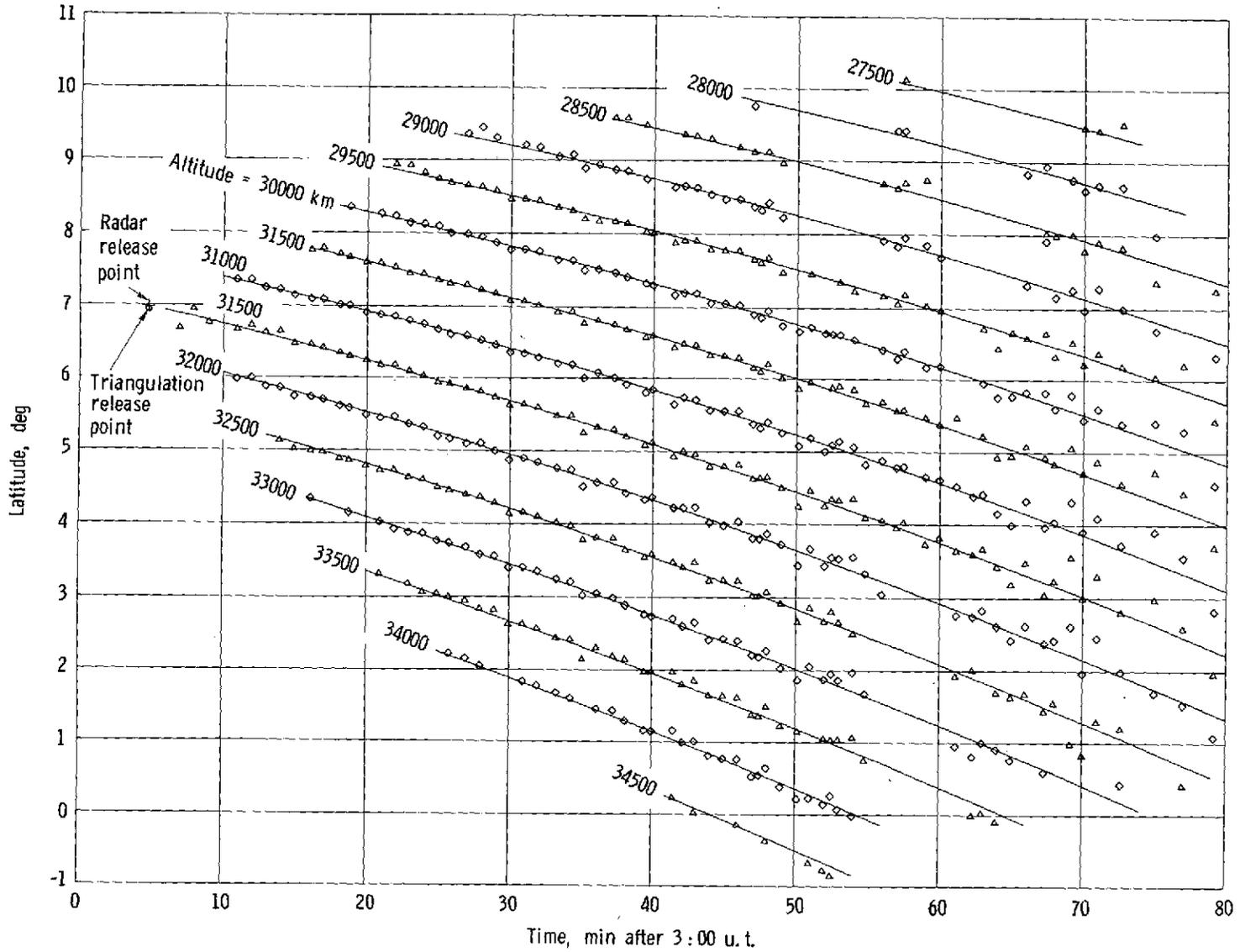
Figure 12.- Latitude of main core as a function of time at selected altitudes.

where h is the altitude in kilometers and t is the time in minutes after 3:00 u.t.   The standard deviation for all the data points kept is 0.078$^{\text{O}}$. The data at later times are gradually degraded because of the difficulty in determining the centerline of the cloud image and because only two sites could be used for triangulation. Table IV shows the standard deviation for the time broken up into three intervals.

TABLE IV.- STANDARD DEVIATIONS MEASURED
IN TRIANGULATED DATA

Time interval, min after 3:00 u.t.	Standard deviation in lat., deg	Standard deviation in long., deg
5 to 35	0.039	0.006
35 to 60	.070	.009
60 to 80	.128	.014

Figure 13 shows this same smoothed data in terms of altitude as a function of latitude for every 10 minutes of time after 3:00 u.t.

Longitude.- The longitude data are fitted by the formula

$$\text{W. longitude} = 73.8955 - 1.9954 \times 10^{-5}h + 0.217102t - 0.0059887t^2 + 9.3235 \times 10^{-7}ht$$
$$+ 2.441126 \times 10^{-4}t^3 - 5.3526 \times 10^{-6}t^4 + 5.780502 \times 10^{-8}t^5$$
$$- 2.49797 \times 10^{-10}t^6$$

where, of a total of 614 points, four points which had errors greater than 0.04$^{\text{O}}$ were discarded. The standard deviation was 0.010$^{\text{O}}$. Table IV shows the standard deviation for the three time intervals.

Because of the greater accuracy obtainable in the determination of the longitude, the data are displayed in a different way in order to illustrate the scatter. Figure 14 shows all of the triangulated points for the longitude as a function of time at an altitude of 31 500 km. The curve is computed from the longitude equation for h equal to 31 500 km. This curve is called the "nominal" curve. The data points relative to this nominal curve for fixed altitude intervals of 500 km are shown in figure 15. For clarity, the altitude interval on each plot is 1500 km. The solid curves are the smoothed or least-squares-fit curves relative to the nominal curve. It may be noted that the formula does not fit the data at very early times in figure 15(a) and the error is about 0.05$^{\text{O}}$ near the release time. Figure 16 shows the same smoothed data with the altitude as a function of longitude at 10-minute intervals.
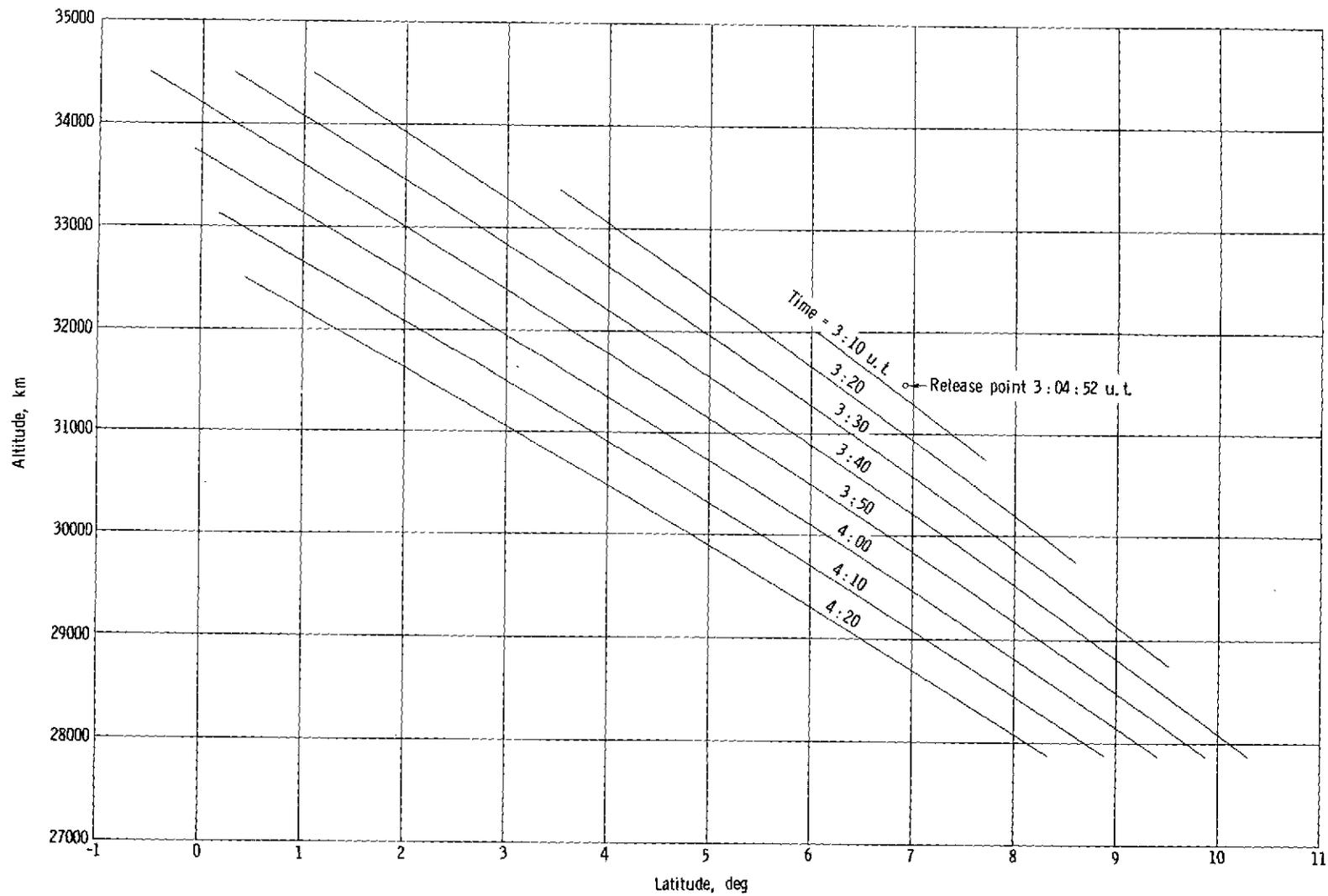
Figure 13.- Altitude of main core as a function of latitude at 10-minute time intervals.
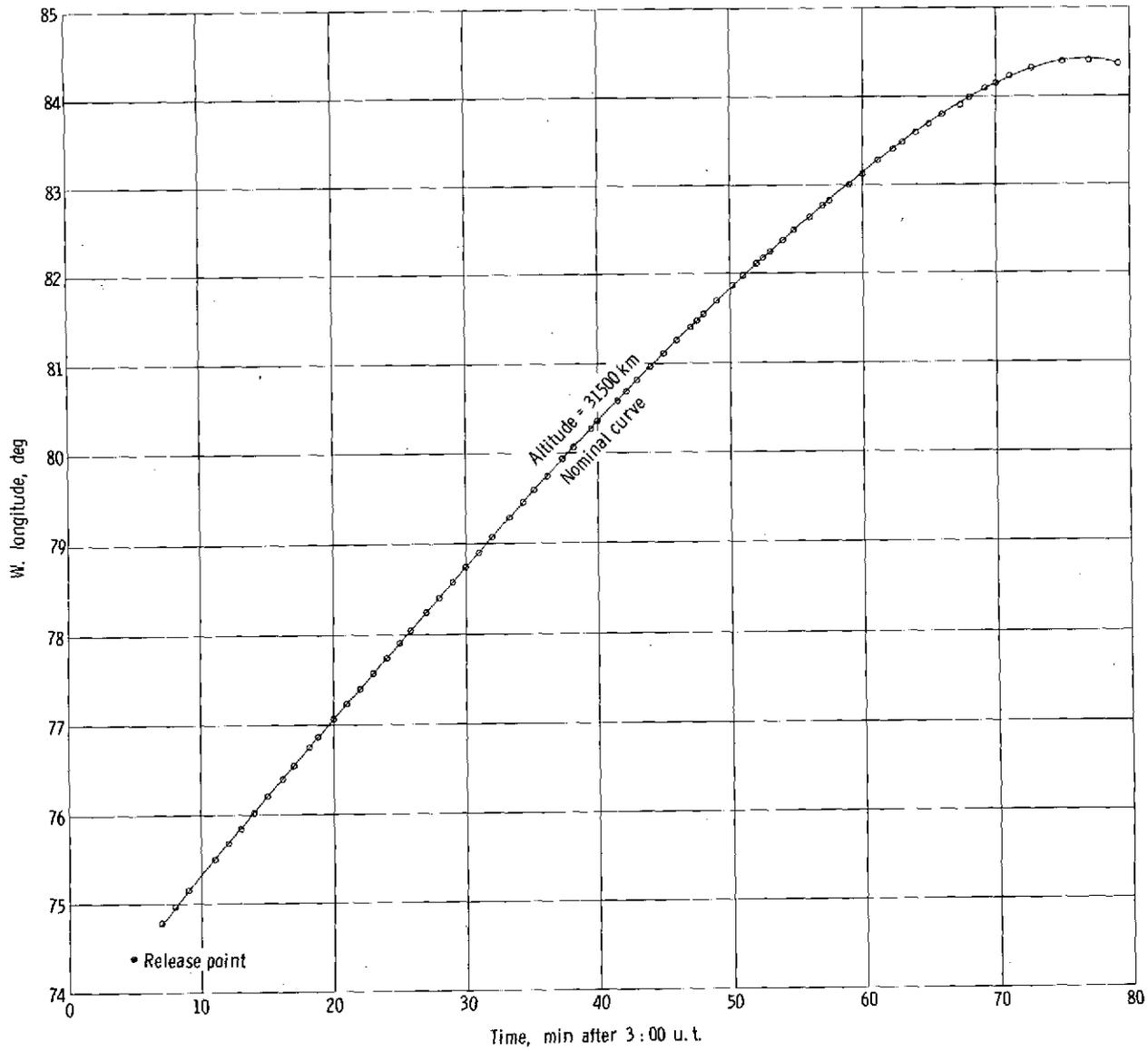
Figure 14.- Longitude of main core as a function of time at 31 500-km altitude.
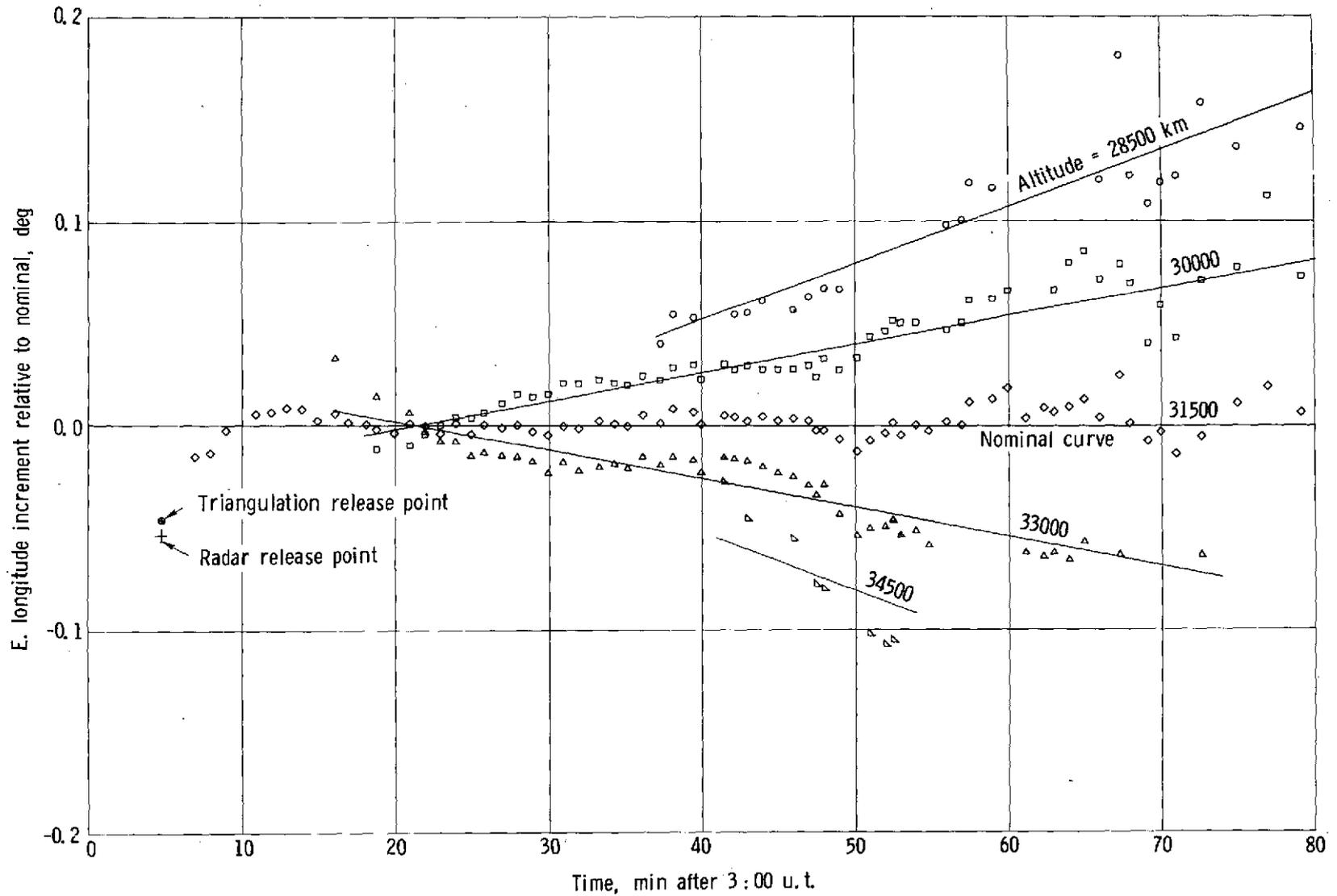
(a) Altitudes of 28 500 to 34 500 km.

Figure 15.- Longitude increment of main core relative to nominal as a function of time at altitude intervals of 1500 km.
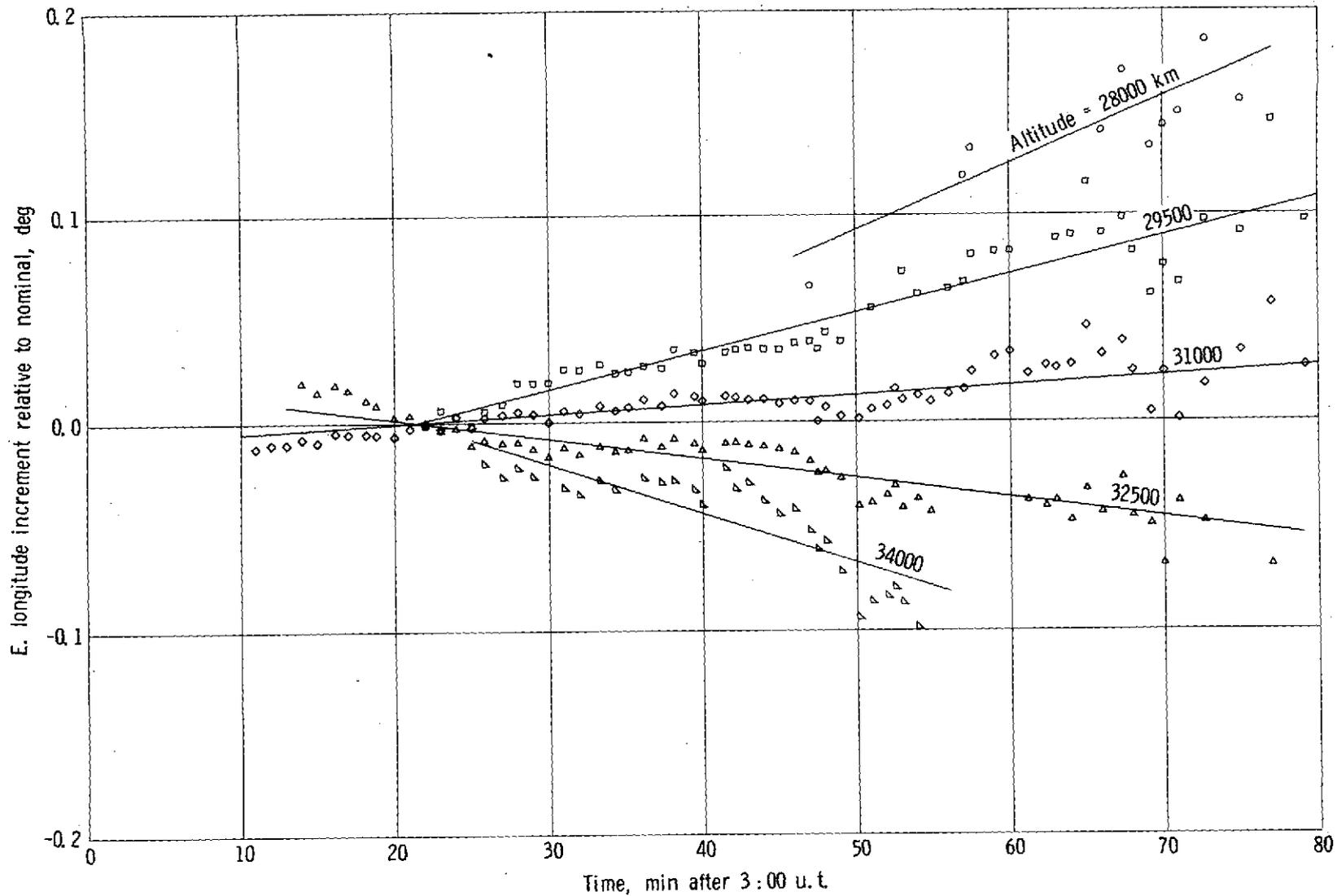
(b) Altitudes of 28 000 to 34 500 km.

Figure 15.- Continued.
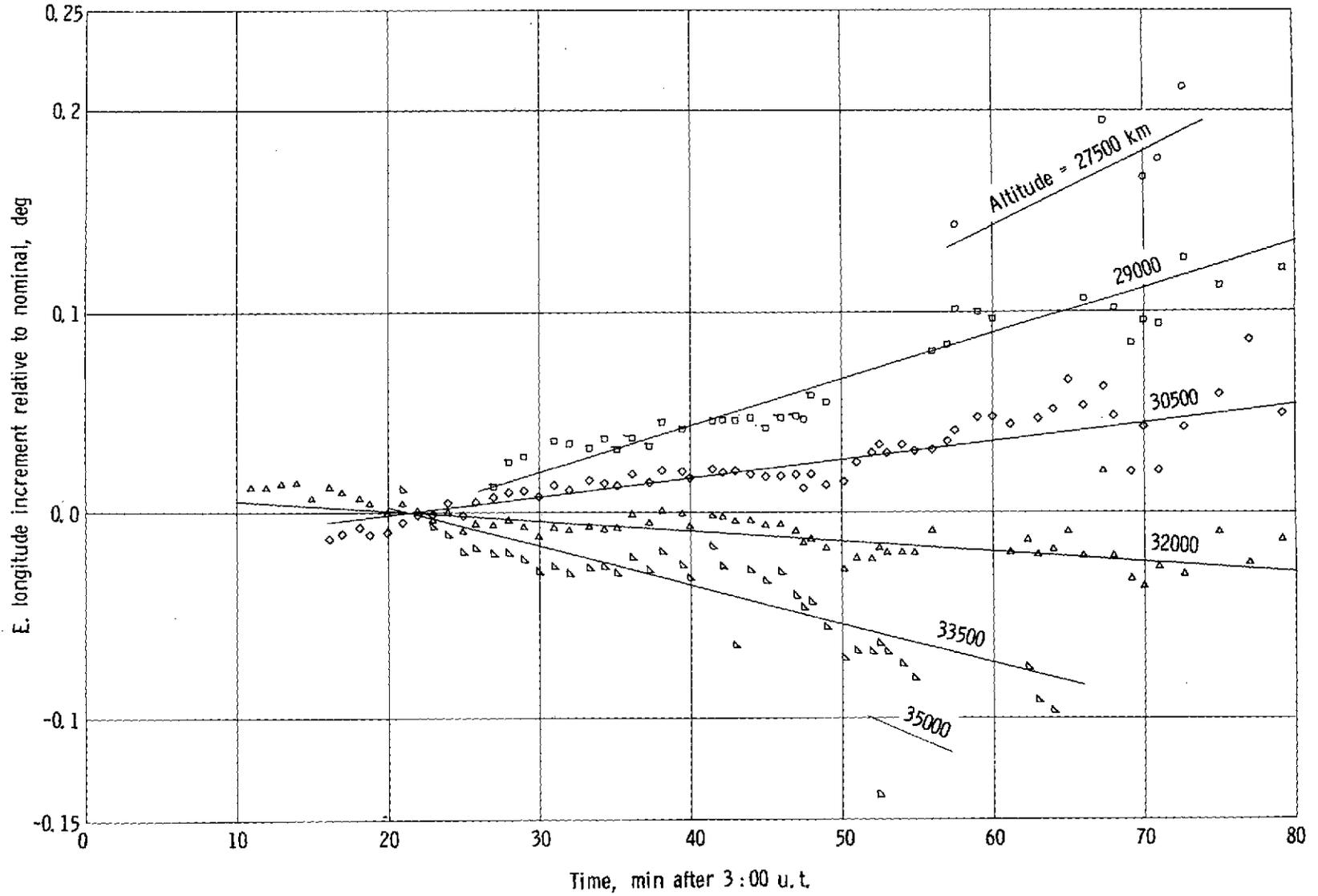
(c) Altitudes of 27 500 to 35 000 km.

Figure 15.- Concluded.
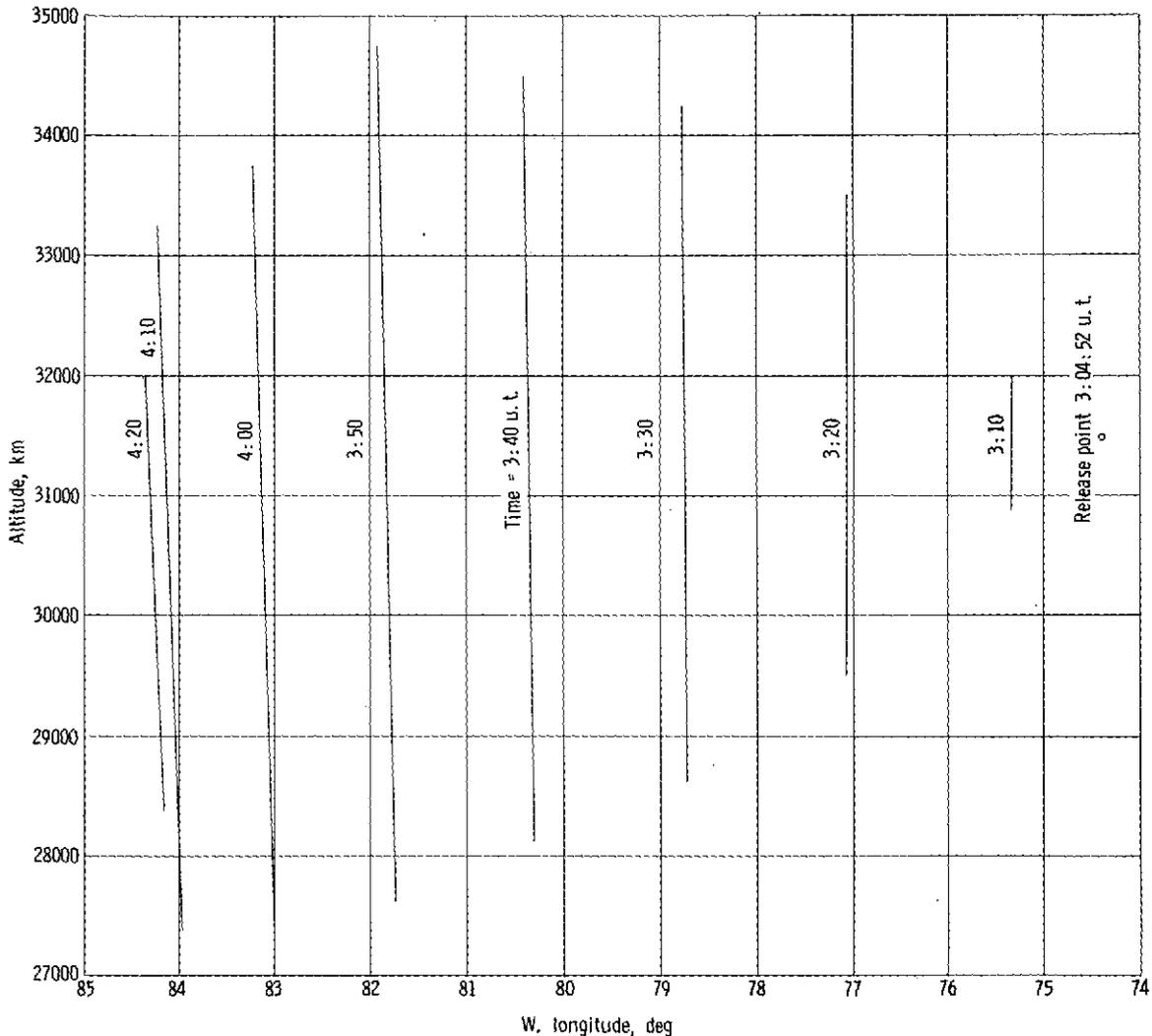
Figure 16.- Altitude as a function of longitude for main core at 10-minute intervals.

Discussion of Errors

Input errors.- Figure 11 depicts the lines of sight from the three triangulation sites to the BIC release point. The smallness of the angles between the lines of sight emphasized the need for making every possible effort to minimize the input errors for the experiment.

The maximum uncertainties in the triangulation-camera coordinates were estimated (ref. 18) to be about 50 m in horizontal distance and about 2.5 m in altitude. After the calibration corrections to eliminate the nonlinearity of the image intensifiers there remained an estimated (ref. 21) residual distortion error of about 0.0025°. Also, it was estimated (ref. 18) that there existed a standard deviation of about 0.0032° in the plate

reader's ability to locate the cloud centerline. This estimate of uncertainty was based on an analysis of one of the better quality photographs. At very early times and especially at late times, the cloud images were less distinct. Also, because of the inferior viewing conditions from the Wallops site, the photographs from there were of lesser quality at all times. Both of these sources increased the uncertainty.

Theoretical triangulation errors.- In references 17 and 18, preliminary studies were made to determine the errors in the triangulation solution of the elongated cloud. These studies used the value of 0.01^o for the line-of-sight input errors. Based on the preceding considerations, this value appears to be realistic. The predicted errors at early times were 0.048^o in latitude and 0.006^o in longitude.

During the experiment useful triangulation data were obtained for 1 hour 15 minutes from Mount Hopkins and Cerro Morado. Because of the somewhat brighter night-sky background at Wallops Island, useful data were obtained from there for only the first hour. The preliminary studies (refs. 17 and 18) revealed that the loss in accuracy of triangulation due to not having Wallops in the triangulation net was about 0.005^o in latitude and about 0.002^o in longitude.

Experimental triangulation errors.- Table IV lists the experimental values for the standard deviations in the latitude and longitude of the barium ion cloud. At early times (5 to 35 min after 3:00 u.t.), the standard deviation in latitude was 0.039^o and the standard deviation in longitude was 0.006^o. These compare very well with the corresponding preliminary theoretical values of 0.048^o and 0.006^o.

The experimental values at later times were not so good as those at the earlier times because the cloud-centerline images were less distinct. From table IV it is seen that at intermediate times (35 to 60 min after 3:00 u.t.), the standard deviations in latitude and longitude were 0.070^o and 0.009^o, respectively. At late times (60 to 80 min after 3:00 u.t.), which was also when Wallops was no longer in the triangulation net, the errors increased further. The standard deviations in latitude and longitude were 0.128^o and 0.014^o, respectively. The average (overall times) standard deviations were 0.078^o in latitude and 0.01^o in longitude.

Disparity With Magnetic-Field-Line Models

The field lines obtained from the barium cloud show a difference from existing models of Earth's magnetic field. For comparison, field-line tracings were made using a model proposed by Cain, Hendricks, et al. (ref. 25) for the main field, with the addition of an external-field model furnished by Mead and discussed in references 26 and 27. This external-field model assumes that the solar wind is perpendicular to the dipole axis with a subsolar distance to the magnetopause equal to 10 Earth-radii, that the front and

back edges of the tail neutral sheet are located at 10 and 40 Earth-radii, respectively, and that the magnitude of the tail field adjacent to the sheet is 40 gammas.

The solid lines in figure 17 are a copy of figure 13 showing the altitude as a function of latitude of the cloud at various times. The field-line tracing of the combined model — going through the point 31 500-km altitude, 5.08° latitude, and 80.36° W. longitude corresponding to a point on the cloud at 3:40 u.t. — is shown by the long dashed line. Table V shows the tabulated data of the line tracing to both extremities of the field line. The angle

TABLE V.- MAGNETIC FIELD LINE WITHOUT RING CURRENT

Altitude, km	Lat., deg	W. long., deg	B_{total}, gammas	B_{north}, gammas	B_{east}, gammas	B_{radial}, gammas
100	54.566	81.548	58 453	-9092	-2 232	-57 698
6 258	44.898	80.241	6 931	-2207	-63	-6 570
13 185	34.685	80.091	1 690	-744	1	-1 518
19 674	25.263	80.150	647	-361	3	-537
26 291	14.896	80.254	289	-200	2	-209
31 500	5.082	80.360	159	-131	2	-91
35 052	-5.178	80.544	101	-97	3	-29
35 534	-15.308	80.951	95	-93	5	16
32 914	-25.103	81.614	134	-116	8	66
28 163	-35.004	82.492	232	-170	14	157
22 274	-44.739	83.623	458	-279	27	362
15 171	-55.279	85.564	1 195	-570	82	1 047
8 398	-65.231	89.576	4 017	-1450	394	3 725
2 276	-74.916	103.659	21 716	-4974	4 180	20 722
100	-77.988	121.142	56 986	-6336	14 861	54 648

between the magnetic field line as delineated by the ion cloud and that predicted by the aforementioned model is 10.5°. The improvement over that given in reference 9, where a 15° difference was reported, is due to the inclusion of the external field.

Implications for Ring-Current Structure

Barish and Roederer (ref. 11) have shown that simple ring currents can be added to give a better agreement of the model with experimental data. A ring-current model similar to theirs was added to the combined model discussed above. The parameters of the
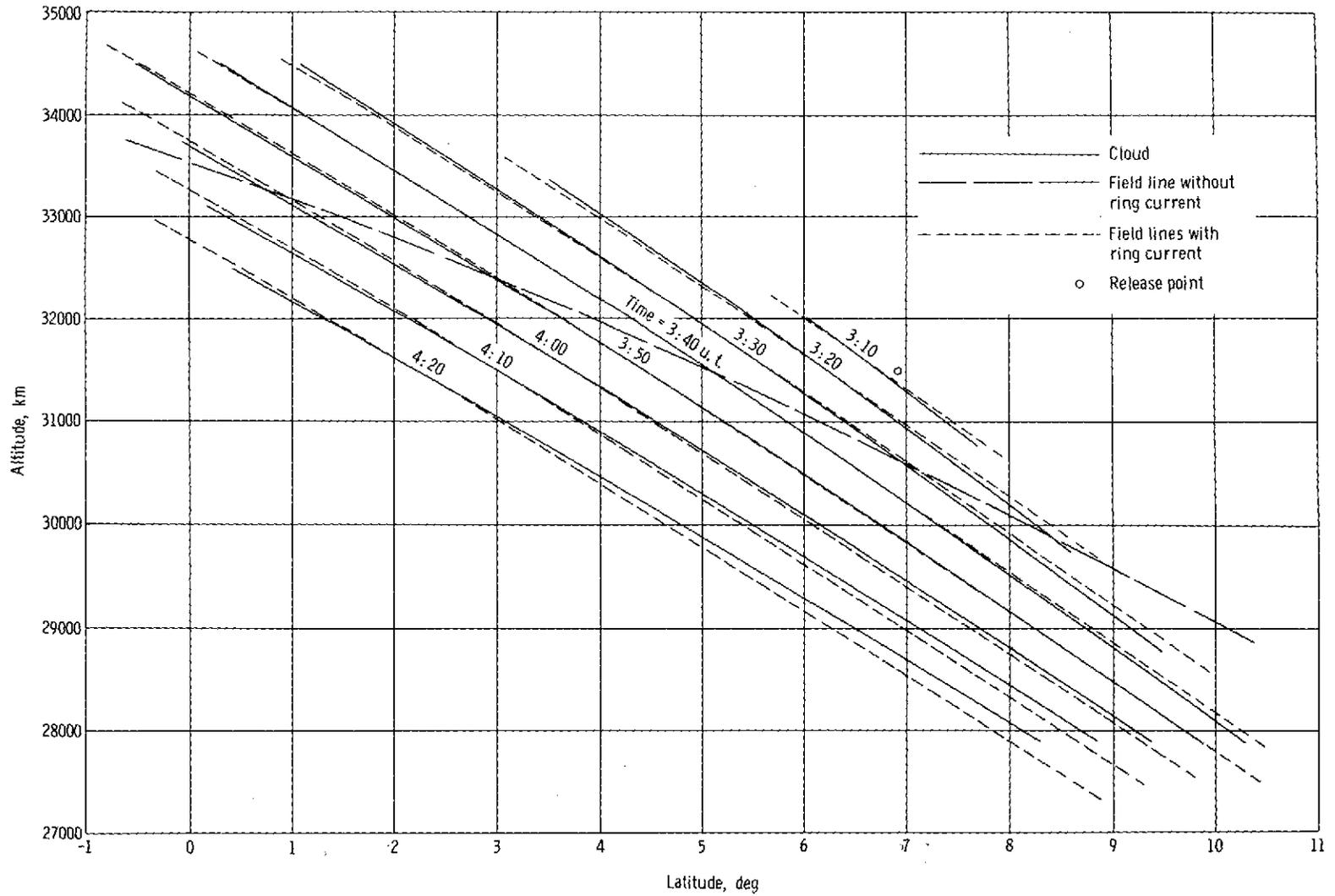
Figure 17.- Altitude as a function of latitude for main core and magnetic field lines.

Barish ring were modified somewhat in order to obtain a slightly better fit to the experimental data. The ring-current model used was made up of 15 rings concentric with the geomagnetic equator, with radii spaced 0.25 Earth-radius apart, with the innermost ring at 5 Earth-radii. The currents in the rings were all equal, except in the inner and outer rings where the currents were one-half of those in the others. The total current was 3.5 MA. The short-dashed lines in figure 17 depict the combined field model with this ring current. Thus, a ring current can account for most of the difference.

Table VI shows tabulated data for the field-line trace with the ring current through the point on the cloud at 3:40 u.t. Figure 18 shows the field-line trace in the meridional plane (radius against latitude).

TABLE VI.- MAGNETIC FIELD LINE WITH RING CURRENT

Altitude, km	Lat., deg	W. long., deg	B_{total}, gammas	B_{north}, gammas	B_{east}, gammas	B_{radial}, gammas
100	52.847	81.474	58 405	-10 083	-2 151	-57 488
4 617	45.112	80.374	10 650	-3 267	-132	-10 135
11 120	34.695	80.120	2 395	-1 008	-4	-2 173
17 729	24.924	80.151	838	-435	3	-717
24 729	14.918	80.249	360	-220	2	-285
31 500	5.082	80.360	188	-133	2	-133
37 121	-4.732	80.538	124	-107	3	-61
38 173	-15.151	80.952	117	-110	6	39
33 630	-24.743	81.590	155	-117	8	102
26 832	-35.066	82.494	286	-184	15	218
20 050	-44.863	83.644	606	-336	34	504
13 179	-54.993	85.598	1 613	-737	113	1 431
6 824	-65.044	89.992	5 626	-2 006	606	5 222
1 180	-74.933	106.787	33 117	-7 046	7 378	31 506
100	-76.630	116.637	57 355	-8 216	15 077	54 724

Figures 19(a) and (b) show the northern and the southern loci of the field-line intercepts with the 100-km-altitude level throughout the lifetime of the cloud. Points on the loci are spaced at 10-minute intervals. The ring current is seen to pull the intercept nearer to the equator in each case.
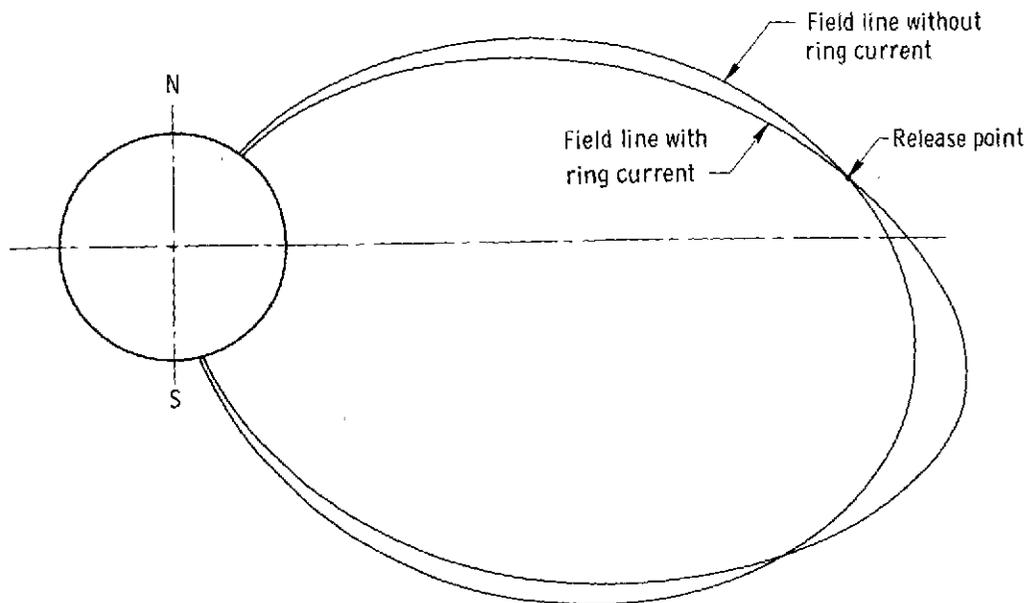
Figure 18.- Magnetic field line, with and without ring current, plotted in meridional plane.
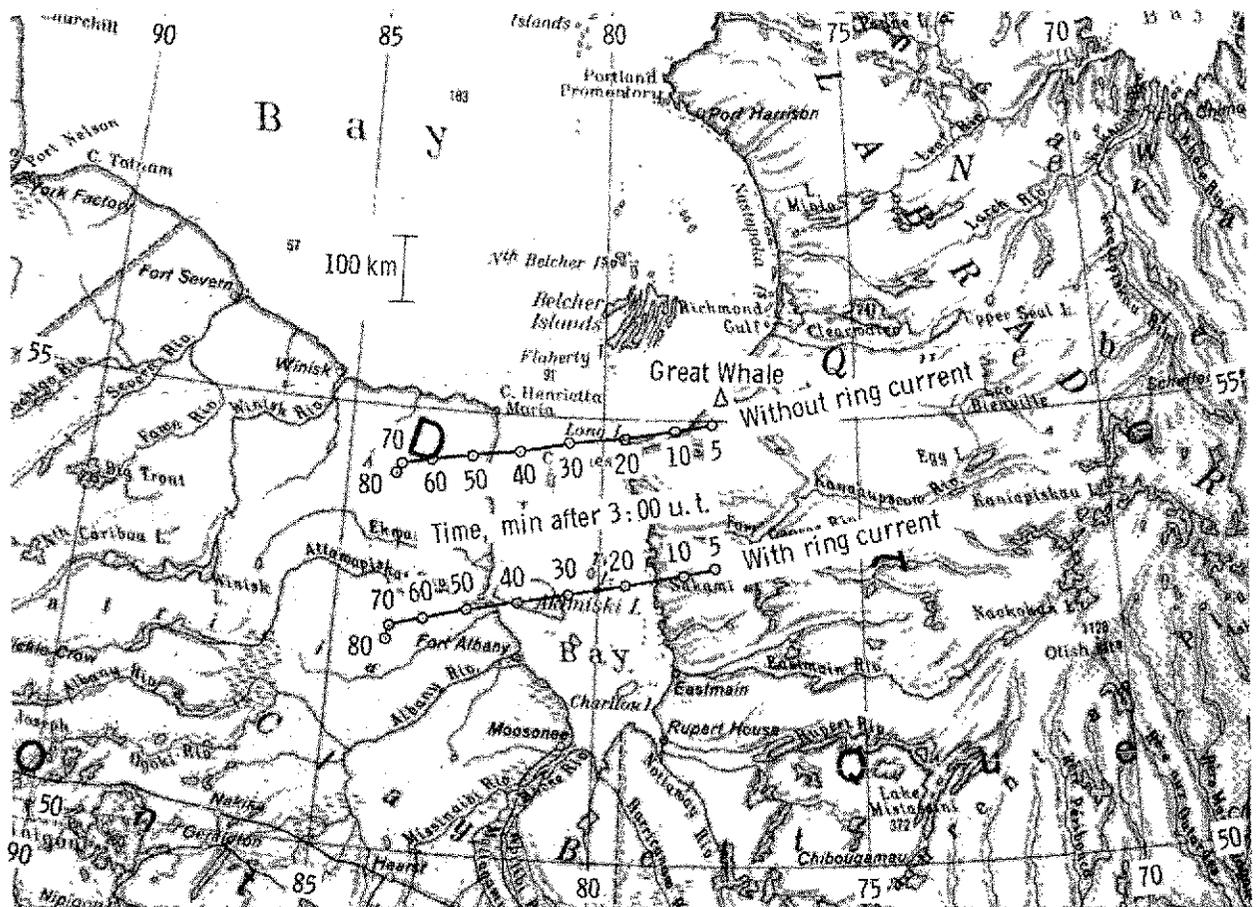
(a) Northern intercepts.

Figure 19.- Loci of magnetic field line intercepts with ionosphere at 100-km altitude.
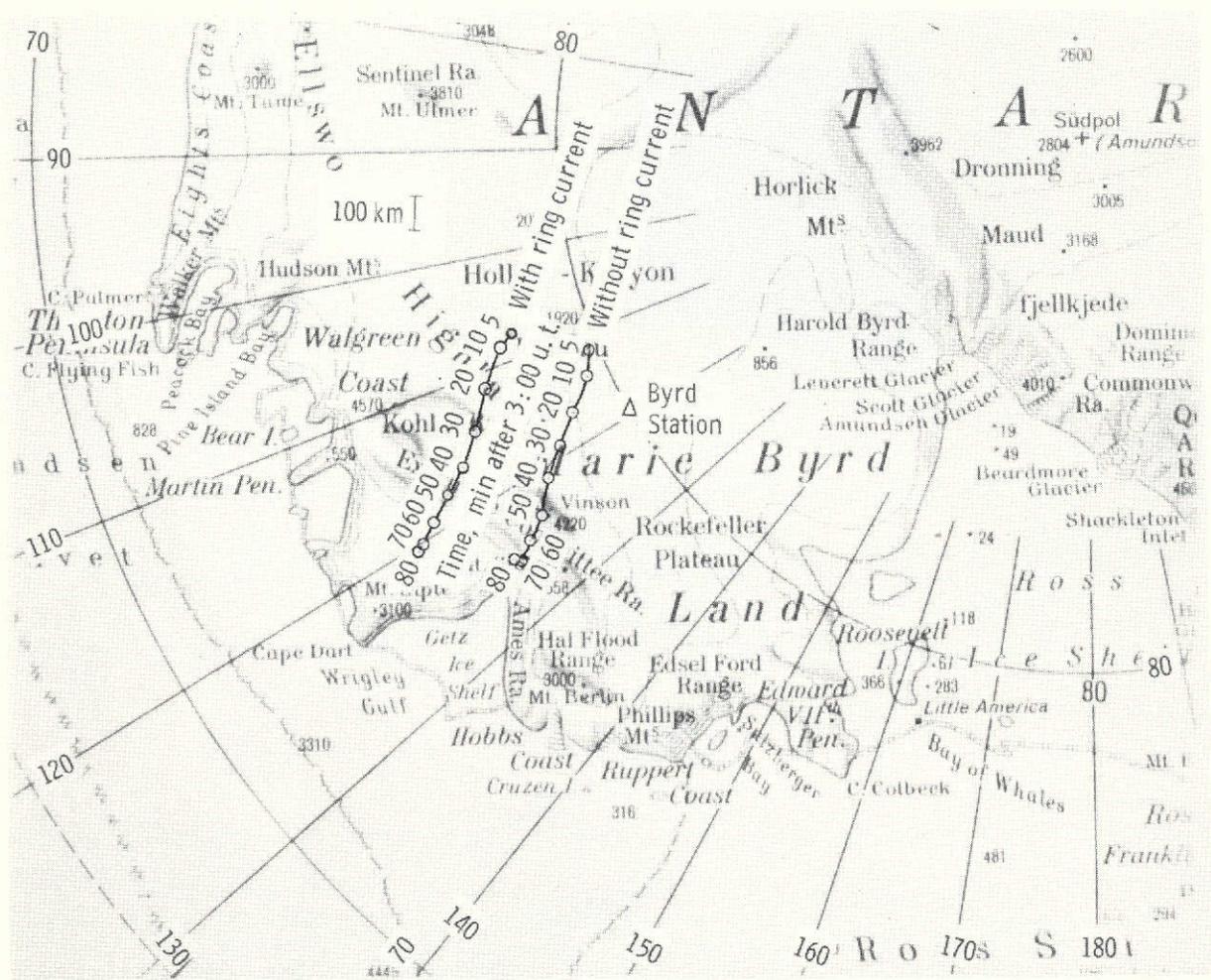
(b) Southern intercepts.

Figure 19.- Concluded.

DRIFT MOTION OF MAIN CORE AND STRIATIONS

Triangulation of Striation Data

The points plotted in figures 20 and 21 show the results of triangulation on striations labeled A, B, C, and D at a fixed altitude of 31 500 km. The photograph inset in figure 20 identifies the striation letter designations. All of the striations appeared to be parallel to the main core, so plots at other altitudes are unnecessary. The smoothed main core is also shown on each plot for comparison. The scatter in the striation data is much more pronounced than that for the main core because the striations were not always well defined. The curves are the result of a smoothing process.

Figure 22 shows smoothed plots of the latitude as a function of longitude and gives a clearer picture of the drift. The points on the curve are spaced at 5-minute intervals.
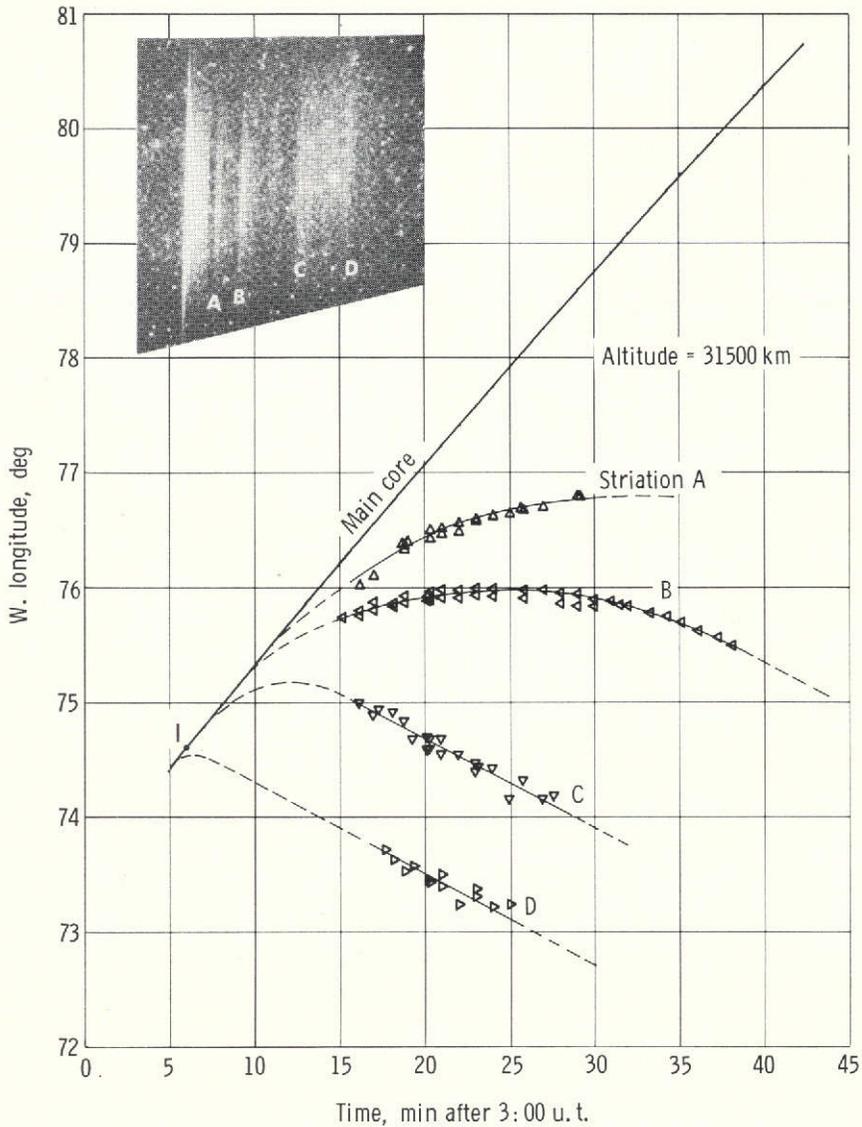
Figure 20.- Longitude of striations as a function of time, at 31 500-km altitude.

The outermost striations C and D acquired identical steady velocities at early times. The striations A and B and the main core all seemed to be approaching this same velocity at the end of their lifetimes. Thus, this drift rate, which the striations and main core approached, must be the velocity of the ambient plasma. The solid lines for the striations in figures 20 and 21 were drawn so as to be consistent with the data points in these figures and also to give consistent smooth curves in figure 22. The dashed curves spaced at 5-minute intervals were an aid in this smoothing.

A least-squares analysis of the longitude data for striation D gives about a 10-percent standard deviation in the measurement of slope. The straight-line intercept of this striation with the main core (point I in fig. 20) gives a definitive time at which the
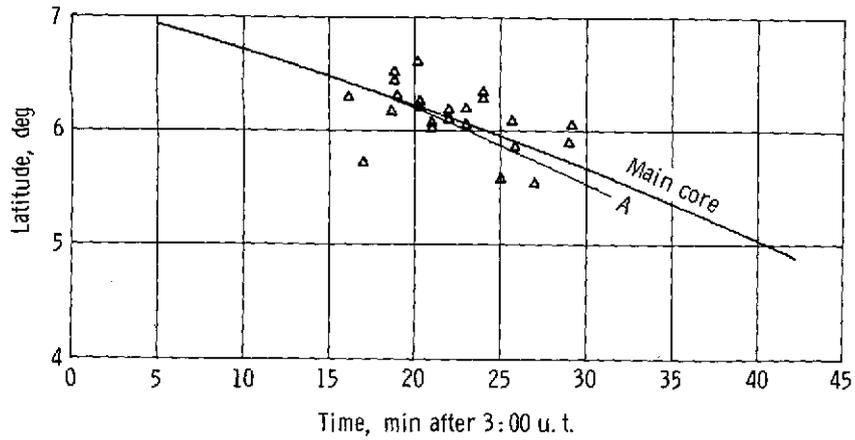
(a) Striation A.
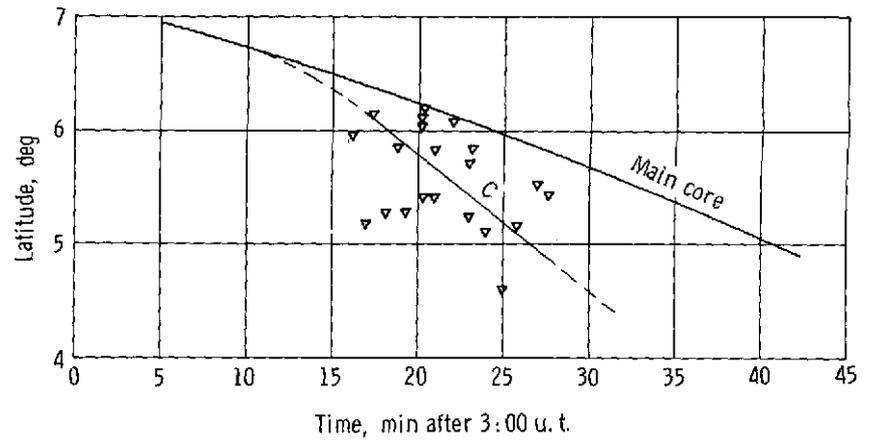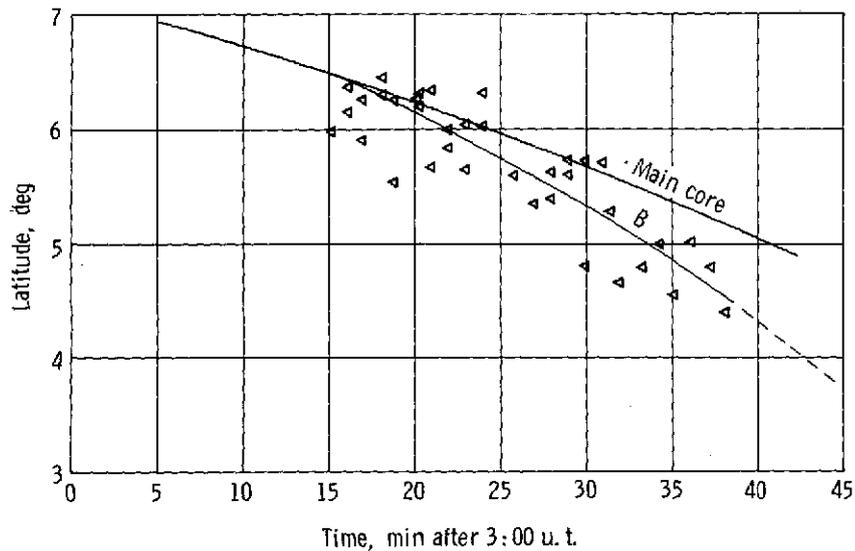
(b) Striation B.
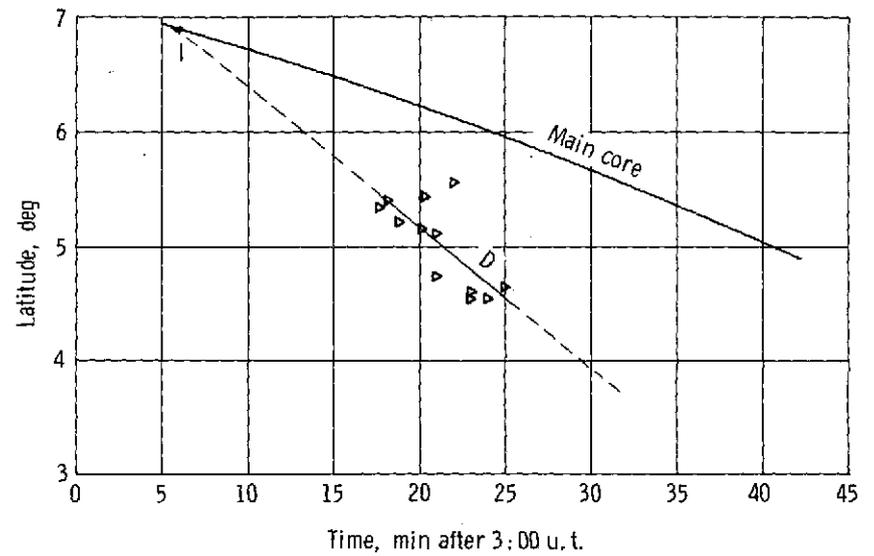
(c) Striation C.

(d) Striation D.

Figure 21.- Latitude of striations as a function of time, at 31 500-km altitude.
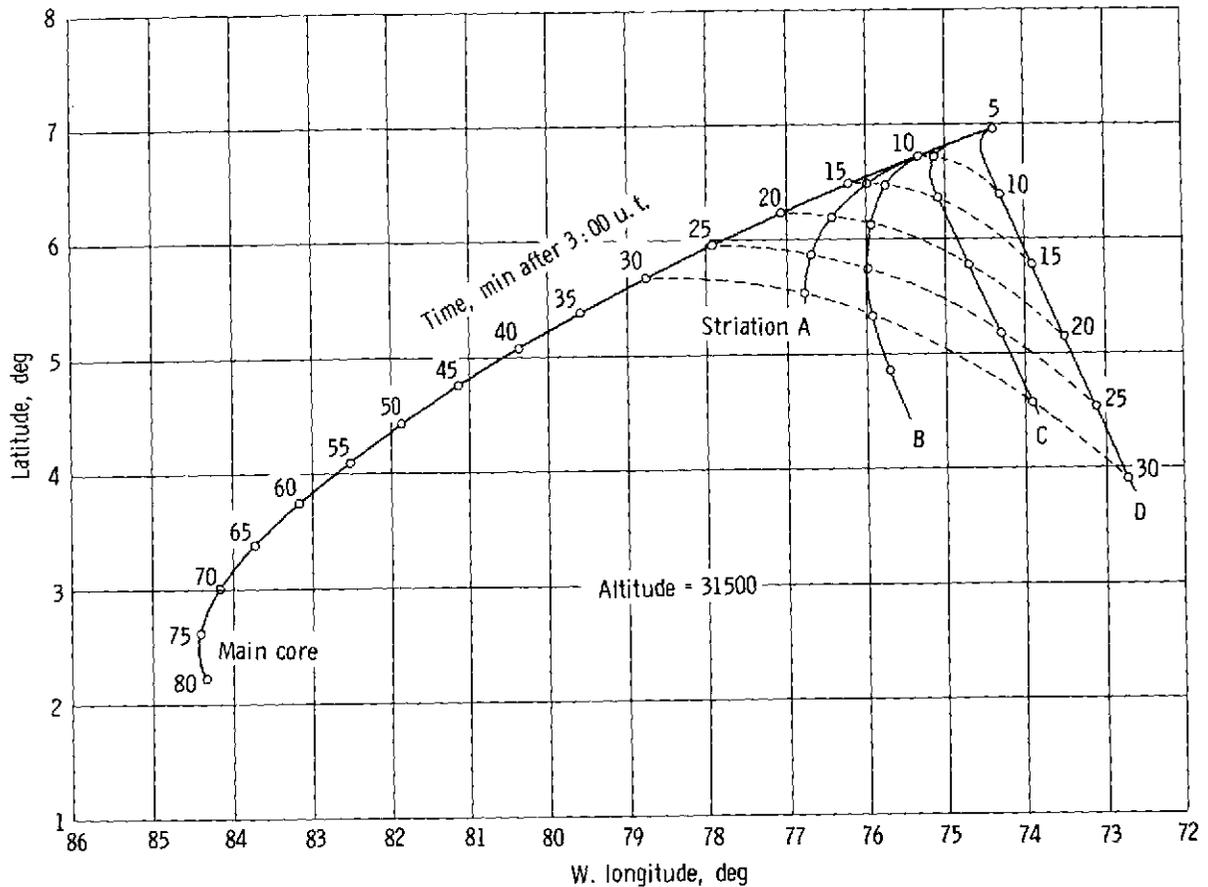
Figure 22.- Latitude as a function of longitude for main core and striations at 5-minute time intervals.

latitude data also may be assumed to intercept the main core (point I in fig. 21(d)). Thus, another datum point is obtained that greatly aids in the determination of the latitude slope and reduces the standard deviation to about 10 percent. The measured drift rates are $-0.00207°$ per second in latitude and $0.00133°$ per second in E. longitude. From this it is deduced that the striation intersection with a spherical surface at an altitude of 31 500 km is drifting, relative to an earthbound observer, to the south at 1.37 km/sec, and to the east at 0.88 km/sec. The rms error in each of these components is estimated to be about 10 percent.

Theory of Deceleration of Ion Cloud

In laboratory experiments (refs. 28 and 29), blobs of plasma projected into a magnetic field initially move freely across magnetic field lines, even though the conditions are such that the field lines permeate the blob interior. This also happens in the case of the ion cloud, as has already been noted in the context of figure 5(a). The question may well be posed why the drift continues after the magnetic field has infiltrated the cloud

interior, in seeming contradiction to the concept of plasma being frozen to the magnetic field lines. By way of explanation, suppose a plasma is projected with velocity v into a magnetic field assumed to be directed out of the plane, as shown in figure 23(a). From the vantage point of a reference frame moving with the plasma, the ions and electrons are initially at rest, and, in addition to the magnetic field, there exists an electric field E directed downward as shown in figure 23(b). Both the ions and the electrons, under the joint action of the magnetic and electric fields, move on cycloidal trajectories as shown. This leads to an effective acquisition of negative charge at the uppermost face and positive charge at the lowermost face. This charge separation in turn gives rise to an electric polarization field within the plasma interior, equal and opposite to that of the ambient field. Interior particles therefore remain at rest, whereas those within the boundary layers at the top and the bottom are subject to only partial screening and drift toward the left. From the reference frame with respect to which the plasma was initially moving with velocity v, it is observed that the interior particles continue to move at this same velocity and at the same time the plasma continues to shed from the lateral faces.

If the release were in a perfect vacuum, the motion would continue until the cloud was entirely consumed through erosion at the boundaries. The situation is modified for an ion cloud released in the magnetosphere, inasmuch as the cloud is immersed in an ambient medium in which the electrons virtually have infinite mobility along the magnetic field lines. It is through the field-alined currents and their closure within the conducting ionosphere (fig. 24) that the polarization charges on the lateral faces of the ion cloud are discharged. As these charges drain away, the polarization field within the cloud interior approaches zero and the velocity of the ion cloud approaches the velocity of the ambient plasma.

(a) Reference frame in which   (b) Reference frame in which plasma is at rest.
    plasma is moving.
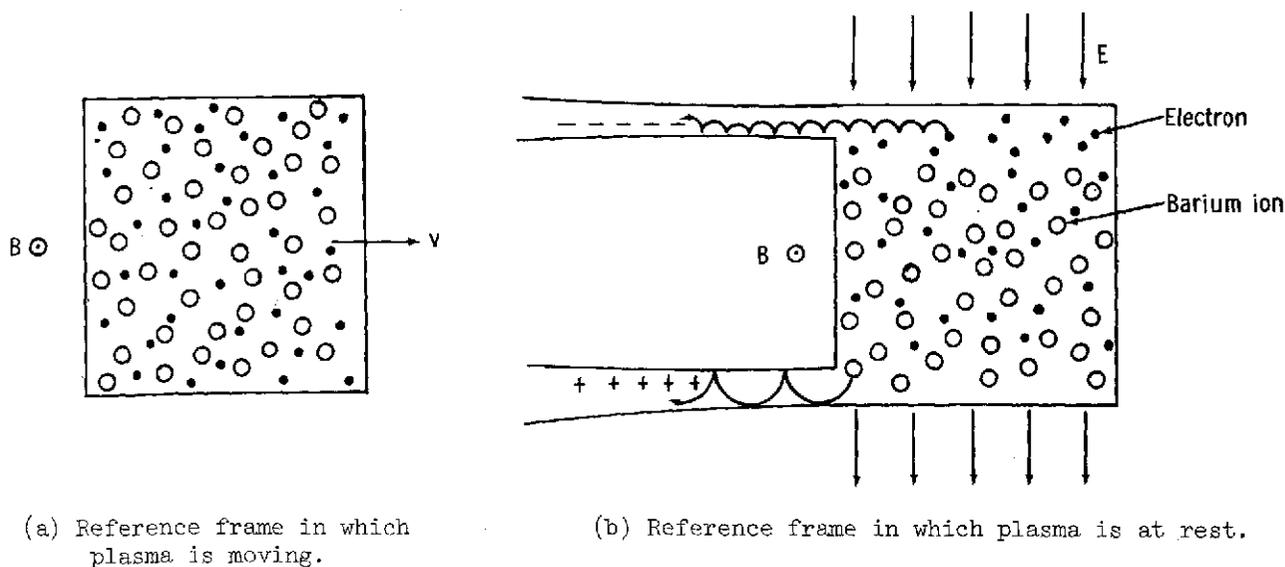
Figure 23.- Mechanism of plasma drift across magnetic field.
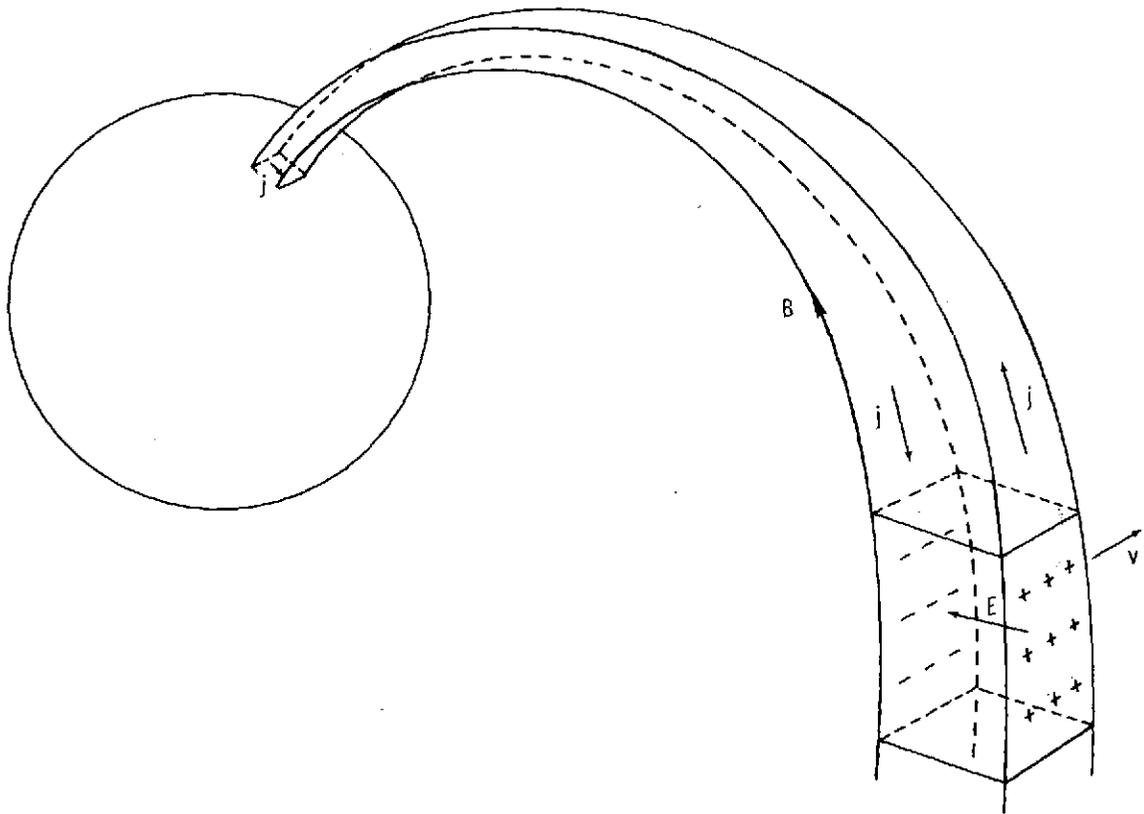
Figure 24.- Magnetic field-alined currents j associated with cloud deceleration.

Disparity Between Theoretical and Observed Decelerations

By taking slopes from figure 20, plots have been prepared (figs. 25(a) and (b)) show-
ing the variation with time of the longitudinal drift rates of both the main core and the
more prominent striational features, identified as A, B, C, and D. Once the striations
have broken away from the main core, their drift-rate curves have an exponential char-
acter, which is what is expected on theoretical grounds (ref. 30). On the other hand, the
deceleration curve of the main core is altogether different in nature which indicates that
the basic underlying mechanism of deceleration is fundamentally different from that oper-
ative in the case of the striations. It is noted that a time delay occurs before the stria-
tions A, B, and C separate from the main core, in spite of the fact that there is abundant
observational evidence that all were formed at early times (refs. 2 and 8). Apparently,
for a while, they remain captive of the main core. There is strong evidence that the
coupling is in the nature of entrainment in the electric polarization wake of the main core.
A more detailed discussion of this concept is given in the succeeding subsection entitled
"Implications for Existence of Polarization Wake." Once the striations have broken loose
from the main core, they seemingly behave thereafter as free agents, exponentially acquir-
ing the velocity of the ambient plasma. In table VII, for each of the striations A, B, C,

44
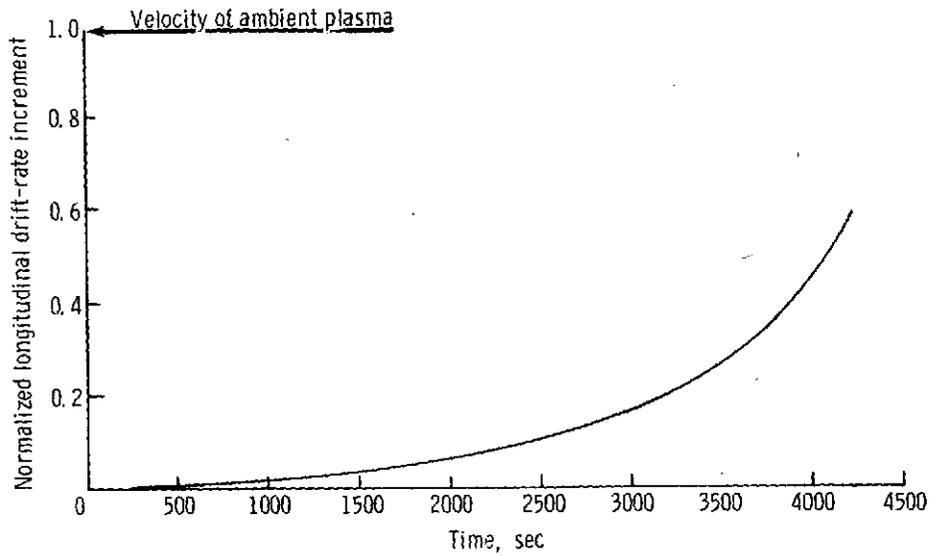
(a) Drift of main core.
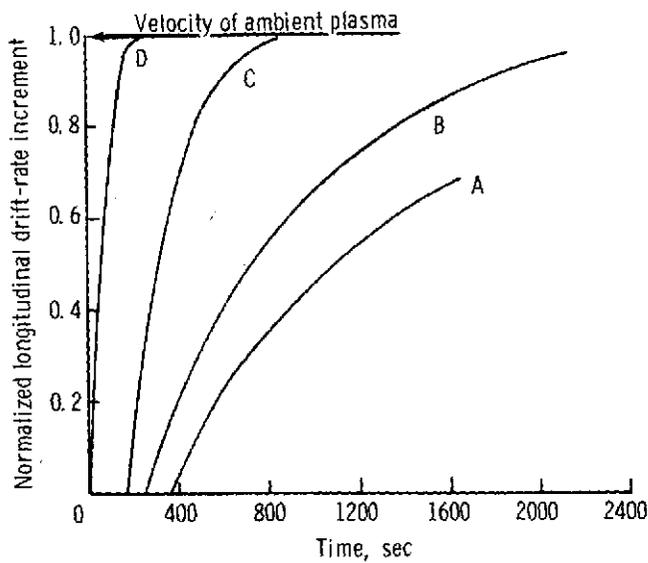
(b) Drift of striations.

Figure 25.- Normalized longitudinal drift-rate increments as a function of time.

and D, values are given for the elapsed time t_0 to break away from the main core together with their exponential deceleration time τ as defined by the equation

$$\Delta \vec{v} = \Delta \vec{v}_f \left[1 - e^{-\left(t-t_0\right)/\tau} \right]$$

where $\Delta \vec{v}_f$ is the drift velocity of the ambient plasma relative to the main core and t is the time after release.

TABLE VII.- BREAKAWAY AND EXPONENTIAL DECELERATION
TIMES FOR VARIOUS STRIATIONS

| Striation	Breakaway time, t_0, sec	Exponential deceleration time, τ, sec
A	390	1000
B	260	650
C	175	200
D	0	80

### Implications for Existence of Polarization Wake

The time lag between the formation of the striations designated A, B, and C and their breakaway from the main core has already been noted. This anomalous behavior is even more forcibly exhibited by the six striational features contiguous to the main core (to which reference has already been made in fig. 5(b)). All of the striations move as though entrained in the wake of the main core. This explanation, on further examination with the aid of figures 26(a) to (d), appears quite plausible. Consider a column of plasma of circular cross section drifting to the left through a tenuous ambient plasma assumed to be at rest. For simplicity, adopt the vantage point of the moving plasma column. In this reference frame the ambient plasma is drifting to the right and the magnetic field is directed into the plane of the paper, as in figures 26(a) and (b). Figure 26(a) depicts the idealized situation corresponding to infinite conductivity. The electric field, in this instance, which drives the ambient plasma must be in the direction indicated. Since the plasma column itself is assumed to be at rest, electrical charge must be distributed on the cylindrical boundary in such a way as to produce a polarization within the column interior, equal and opposite to the electric field at infinity. The resultant electric field is represented by the broken lines and the associated convective flow by the unbroken lines in figure 26(a). It is noted that the ambient plasma, with the entrained magnetic field lines, parts as the column approaches and closes behind it once it has passed. The flow is similar to that of an inviscid fluid around a cylinder of circular cross section (fig. 26(c)). However, as is well known in aerodynamics, the existence of the slightest amount of viscosity changes the flow pattern radically to that depicted in figure 26(d). It is noted that a portion of the fluid, in this example, is entrapped behind the cylinder and that at its boundaries there exist vortex sheets (which have been shed from the cylinder as boundary layers) of opposite sign, which merge and cancel at the cavity closure point. This vorticity can be pictured as driving the fluid within the wake to keep pace with the moving cylinder. Analogously, in the plasma example, if finite conductivity is assumed, there is a continual shedding of charge of opposite sign at the lateral faces of the main

46
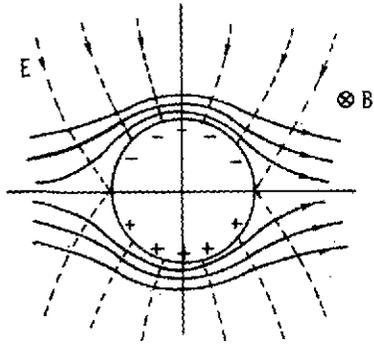
(a) Infinitely thin charge layer in flow around plasma column.
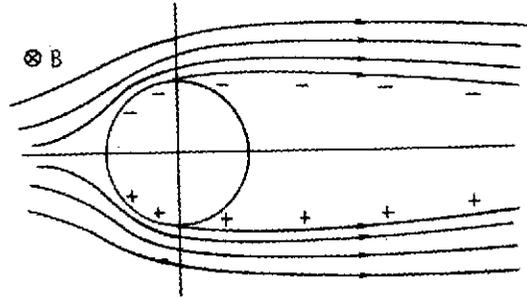
(b) Charge layer of finite thickness in flow around plasma column.
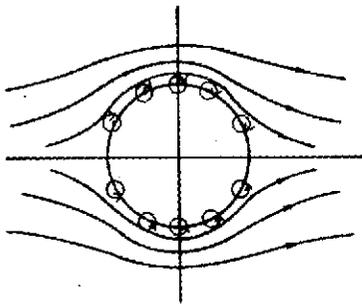
(c) Infinitely thin vortex layer in fluid flow around cylinder.
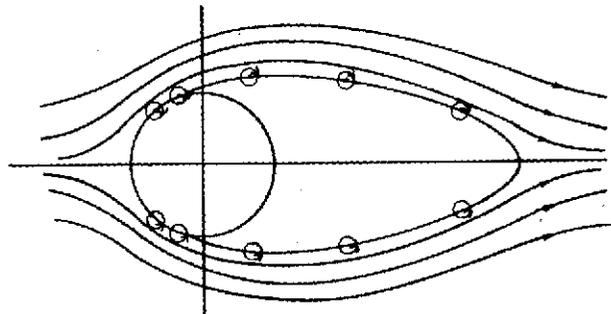
(d) Vortex layer of finite thickness in fluid flow around cylinder.

Figure 26.- Plasma and fluid wake flows.

core (fig. 26(b)). Between these charged sheets, which have a thickness equal to approximately a Debye length, there exists an electric polarization field which, coupled with the magnetic field, drives the entrained plasma along with the parent column. Only when the striations have broken free from the wake would they rapidly acquire the velocity of the ambient plasma. One difference between the fluid and plasma flows pertains to the length of the wake. In the fluid flow the cavity length is of the same order of magnitude as the cylinder diameter, closure being effected through random thermal motions of the particles. In the plasma flow, on the other hand, the motion of charged particles perpendicular to the magnetic field lines is severely inhibited and as a consequence the plasma wake can extend to a considerable distance downstream.

The existence of such a wake not only provides an explanation for the anomalous motion of the striational features, but also serves to explain why the deceleration of the main core differed markedly in nature from that of the striations and why it was more rapid than that theoretically predicted (based on the formulas of ref. 30). Thus, some of its momentum would be imparted to the ambient plasma entrained within the wake cavity.

In addition, the existence of such a wake would increase the area of interaction and, hence, the resistive dissipation at ionospheric levels.

DETERMINATION OF ELECTRIC FIELD

Calculation of Electric Field From Striation Drift

The outermost striational features designated C and D achieved a steady velocity within a few minutes, indicating that they had thus acquired the velocity of the ambient plasma. Striation D acquired a steady drift within 2 minutes of the release. Striation C took somewhat longer, acquiring a steady velocity after about 10 minutes. Each permitted accurate triangulation and provided convective-drift data over the period 3:15 to 3:30 u.t.

From the measurement of the drift of the intercepts of the striations with surfaces of constant altitude as described in the section "Drift Motion of Main Core and Striations," the drift perpendicular to the magnetic field lines can readily be calculated. This drift has been resolved into two components, one within the plane of the field line, henceforth referred to as the meridional component, and one perpendicular thereto. Since the release was made very close to the prime magnetic meridian the plane of the magnetic field line passing through the release almost exactly coincided with the geographic meridian and it seemed appropriate therefore to express this perpendicular component as easterly or westerly, as the case may be.

Relative to an inertial frame the striation drift had a meridional component of 0.995 km/sec inward and a perpendicular component of 3.62 km/sec to the east. By invoking the MHD approximation and assuming an ambient magnetic field $\vec{B}$ of 188 gammas, the electric field $\vec{E}$ can be computed from the equation

$$\vec{E} = -\left(\vec{v} \times \vec{B}\right)$$

A meridional component of 0.68 mV/m inwards and a component directed to the west of 0.19 mV/m were obtained for the electric-field vector in the proximity of the release relative to an inertial frame. (Relative to a coordinate system rotating with Earth the inward meridional component was equal to 0.17 mV/m, the westerly component remaining unchanged.) These values are about 20 percent higher than those given in the preliminary report on the BIC experiment (ref. 9). Most of this difference is attributable to the revised value of $\vec{B}$ that resulted from the incorporation of the ring current. By assuming that the magnetic field lines are lines of constant electric potential and by approximating the magnetic field by a dipole field, the electric field in the proximity of the cloud was mapped onto the ionosphere and into the magnetic equatorial plane by using expressions

derived in appendix B of reference 9. The expressions for the meridional and azimuthal components $\left(E_M \text{ and } E_A, \text{ respectively}\right)$ are

$$\frac{E_M(\lambda)}{E_M(0)} = \frac{\left(4 - 3 \cos^2 \lambda\right)^{1/2}}{\cos^3 \lambda}$$

$$\frac{E_A(\lambda)}{E_A(0)} \approx \frac{1}{\cos^3 \lambda}$$

where λ is the magnetic latitude (equal to 16.0° at 31 500 km and 64.3° at the iono-spheric altitude of 100 km). The results are summarized in figures 27(a) and (b) for the Earth-centered and the inertial reference frames, respectively.

(a) Earth reference.   (b) Inertial reference.
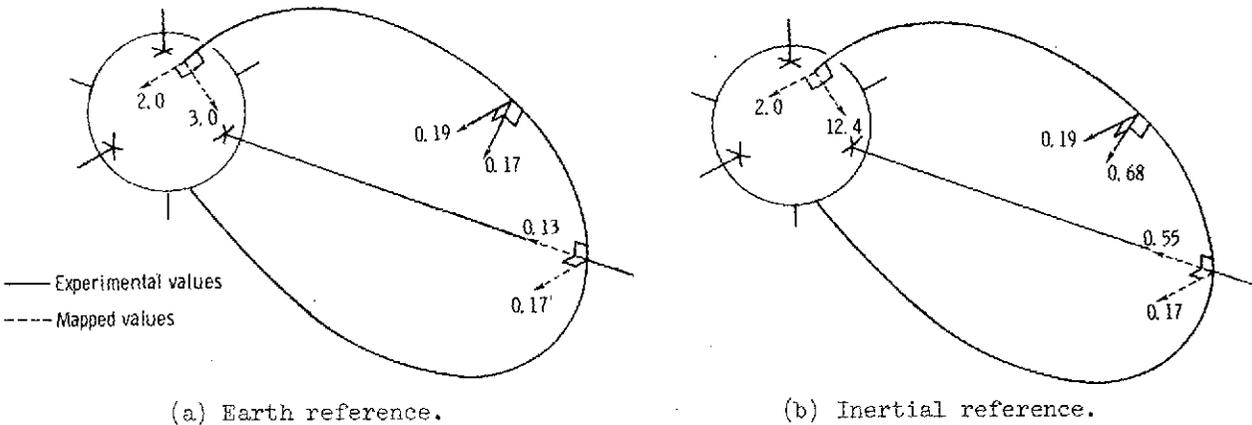
Figure 27.- Electric-field components in mV/m.

Justification for Neglecting Gravitational Drift

In computing the electric field it was assumed that the drift was wholly attributable to electric forces. This is not quite true. Under the pull of gravity the electrons migrate to one side of the cloud and the ions to the other, producing an internal polarization field. If the release had been in a perfect vacuum, this internal polarization field would have allowed the cloud to fall with the local gravitational acceleration (ref. 31). In practice, the space-charge buildup at the lateral faces is inhibited through field-alined currents, and under these circumstances it is found that a terminal velocity is reached with a steady current flowing through the cloud interior sufficiently large to produce a $\vec{j} \times \vec{B}$ force, equal and opposite to the pull of gravity.

The vertical fall of an elongated and featureless cloud cannot, of course, be distinguished from a southward drift resulting from an eastwardly directed electric field. From the theory developed in reference 30 one can deduce that the velocity of an ion cloud falling under gravity is given by

$$v = g\tau\left[1 - \exp\left(-\frac{t}{\tau}\right)\right]$$

where τ is the exponential deceleration time as given in table VII. For the BIC release, the local acceleration due to gravity g was about 0.272 m/sec^2. Because both the cloud main core and the striations were inclined at about 45° to the horizontal, the effective acceleration perpendicular to the cloud axis was 0.193 m/sec^2. For the striations C and D, the exponential deceleration times were 200 and 80 seconds, respectively (table VII). The corresponding terminal velocities of fall under gravity were therefore 0.038 and 0.015 km/sec. Because the centrifugal force, which has thus far been neglected, tends to alleviate the effects of gravity and leads to further reductions in the estimate of the terminal velocity (given above), the entire transverse drift of these striational filaments can be attributed to the ambient magnetospheric electric field.

Comparison With Magnetospheric Convection Models

In figures 28(a) to (d) various predictions that have appeared in the literature (refs. 32 to 34) pertaining to the convective flow in the magnetic equatorial plane are presented. Actually, the contours are equipotential lines at 5-kV increments. With the MHD approximation, however, these coincide with the streamlines of the convective flow of the thermal plasma. Figures 28(a) and (b) are based on theoretical calculations by Wolf (ref. 32) in which he invokes certain assumptions regarding the distribution of ionospheric conductivity. In figure 28(a) the magnetic field lines entrained by the solar wind are assumed to be antiparallel to Earth's field lines in the proximity of the nose of the magnetopause, resulting in field-line merging. Those geomagnetic field lines tied to the interplanetary field lines are dragged back over the polar caps by the streaming solar wind, subsequently reconnecting in the far tail. Figure 28(b) differs from figure 28(a) in that the interplanetary field is assumed parallel to the geomagnetic field at the nose. For this there is no field-line merging over the forward portion of the magnetopause and the boundary. Stresses producing the convective flow are viscous in nature. Figure 28(c), from reference 33, was obtained by mapping the ionospheric electric field, which drives the DS ionospheric current system, onto the equatorial plane, by assuming the magnetic field lines to be lines of constant potential. Figure 28(d) (ref. 34) shows the convective flow hypothesized by Brice on the basis of his analysis of diverse observational data pertaining to proton and electron precipitations, motions of auroral structures, ionospheric
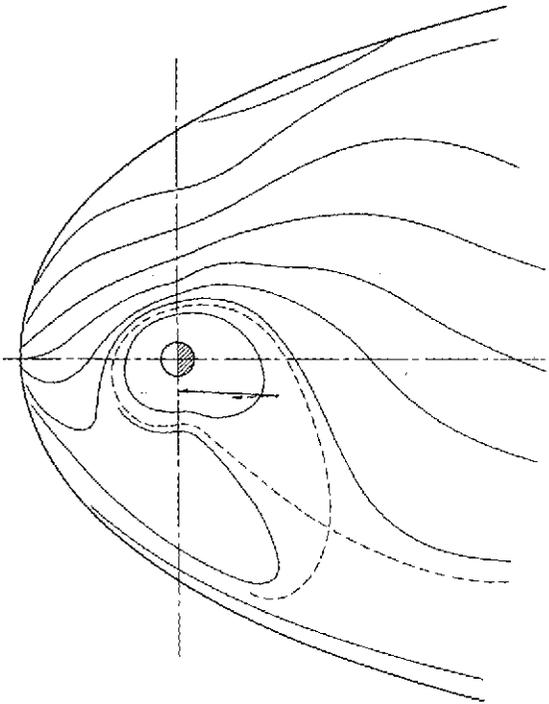
(a) Wolf model - field-line merging (ref. 32).
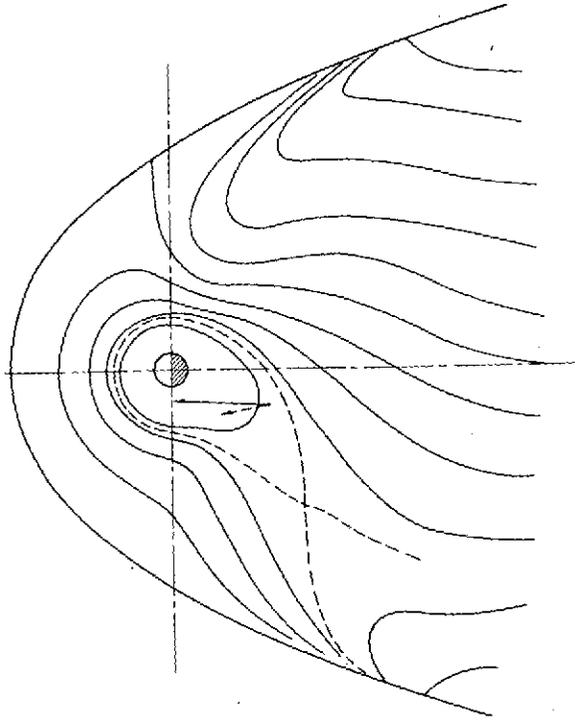
(b) Wolf model - no field-line merging (ref. 32).

———————— BIC measurements

— — — — — Model predictions

⊢————————⊣ 3 mV/ m
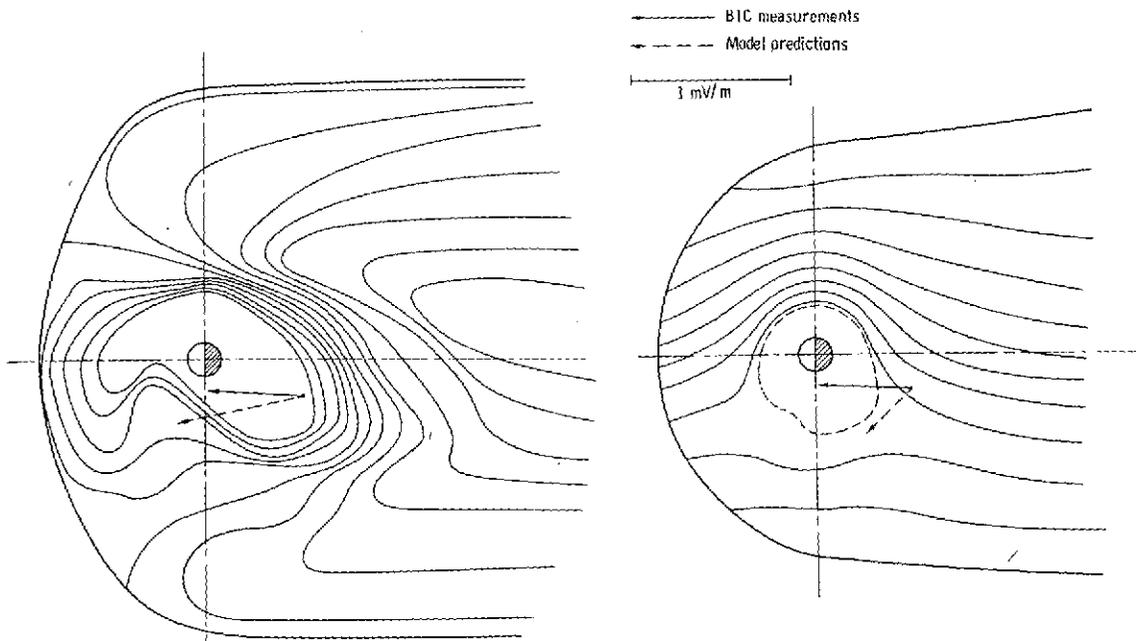
(c) Taylor and Hones model (ref. 33).

(d) Brice model (ref. 34).

Figure 28.- Comparison of measured electric field with magnetospheric models within magnetic equatorial plane.

currents, etc. In each instance, the electric field in the proximity of the cloud has been mapped along the magnetic field line down to the magnetic equatorial plane and compared with the electric-field vector at the same equatorial location as predicted by the various models shown in figure 28. It is noted that, in each instance, the experimentally determined field is more radially oriented, implying a more nearly azimuthal convective flow. The direction of plasma flow is very important in geophysics, since a radial drift results in energization of the plasma, whereas an azimuthal drift does not. This predominantly azimuthal convective drift suggests that the release at L = 7.1 was, if not within, at least closer to the boundary of the plasmasphere than had been expected. (It is known that at times of magnetic quiet the plasmasphere becomes increasingly distended.) Carpenter, on the basis of the limited whistler data taken at the time of this experiment, estimated that the plasmapause had an L-value of between 4 and 4.5 (ref. 6) but he also remarked "the barium release took place within $\approx15^{\circ}$ to 40° in longitude of some irregular plasmasphere structure which may have extended to larger L-values than those indicated by the limited whistler data."

Comparison With Simultaneous Balloon and Whistler Measurements

The ionospheric electric field, measured at the time of the experiment from balloons launched from Great Whale (ref. 6) and averaged over the 30-minute interval following release, had an eastward component of 4 mV/m and a northward component of 12 mV/m. Since a northward ionospheric electric field is required to drive an eastward Hall current and also an eastward ionospheric field is required to drive an eastward Pedersen current, these balloon measurements appear to be qualitatively consistent with the existence of an eastward current flowing somewhat to the south of Great Whale, as inferred from magnetometer records taken at Great Whale, Resolute, and Ottawa (ref. 5). Mapping the average ionospheric electric field as determined from these balloon measurements onto the magnetic equatorial plane under the assumption that field lines are equipotentials yields the following field strengths relative to a rotating Earth: an average eastward component of 0.3 mV/m and an average radially outward component of 0.4 mV/m. These equatorial fields are almost diametrically opposed to those deduced from the BIC experiment (fig. 27(a)).

The BIC experiment, on the other hand, appears to be generally consistent with the whistler measurements made at Great Whale, Roberval, and Byrd Station. In figure 29 the westward components of the equatorial electric field as deduced from the BIC experiment, whistler measurements, and balloon measurements over the 30-minute interval following release are compared. Error bars are given for both the BIC and whistler measurements. No error bar is available for the balloon measurements.

The possibility is raised in reference 6 that the disparity between the ground-based magnetometer and balloon measurements, on the one hand, and the BIC and whistler mea-
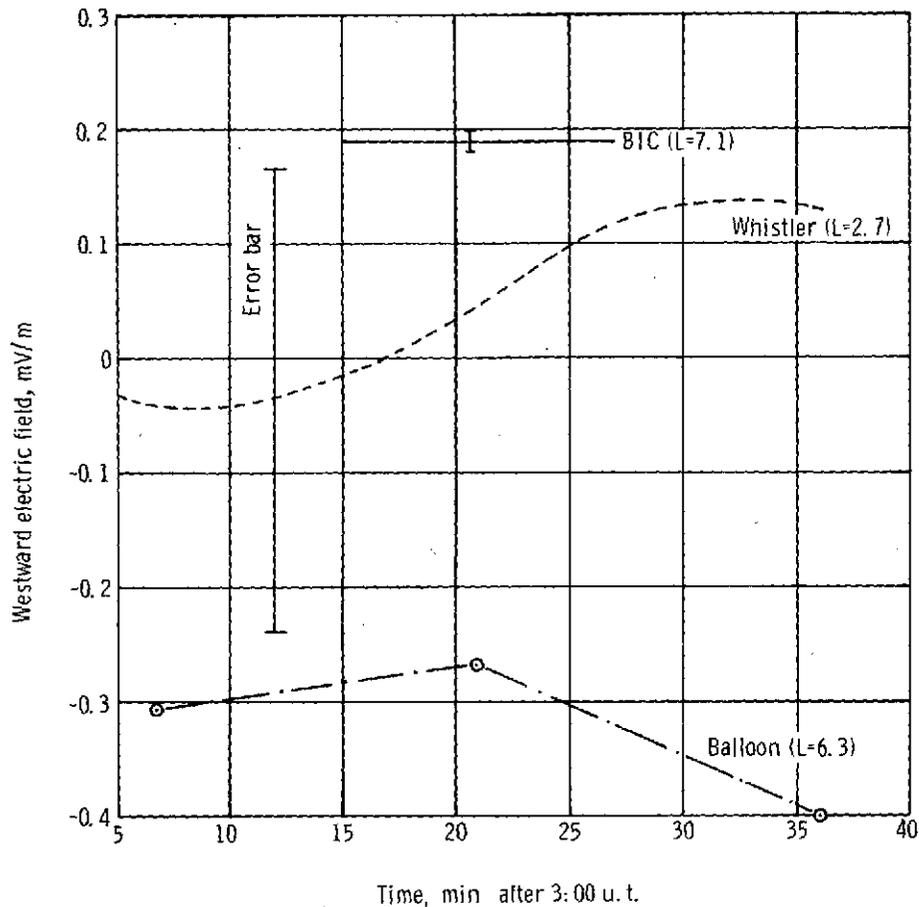
Figure 29.- Comparison of westward components of equatorial electric field.

surements of electric fields, on the other hand, may be attributable to electric-field variations from one magnetic field line to another, though the individual field lines remain equipotentials. This, however, seems unlikely in that the balloon measurements appear to be consistent with the magnetometer measurements taken at widely dispersed geomagnetic observatories, and in that the BIC and the whistler measurements are mutually consistent, in spite of the large separation in the L-shells to which they refer. It seems much more plausible to attribute the disparity to the existence of potential differences along the field lines. If such gradients do exist, it raises serious questions regarding the validity of the frequently used procedure of mapping, along magnetic field lines, ionospheric fields onto the equatorial plane and vice versa.

REVIEW OF GROUND-BASED DATA

General Considerations

Correlative geophysical measurements were made at a number of ground-based stations during the BIC experiment. Most of them were made at the Great Whale

Geophysical Observatory at the mouth of the Great Whale River in Quebec, Canada. In addition, balloons were launched from Great Whale carrying instruments to measure electric fields and X-rays. Figure 19(a) is a map of the lower portion of the Hudson Bay and the surrounding territory showing the location of the Great Whale Geophysical Observatory and two predictions of the locus of the northern extremity of the field line (100-km altitude) threading the ion cloud. The one closest to Great Whale was computed using the field-line tracing program (without ring current) and was made in the planning phase of the experiment and the other, displaced from the first by about 200 km, incorporates the effect of the ring current as discussed in the subsection entitled "Implications for Ring Current Structure." A map showing the locus of the southern extremity of the field line in relation to Byrd Station, Antarctica, is presented in figure 19(b). The effect of the ring current is to displace the extremity of the field line by about 250 km away from Byrd Station.

Geophysical Conditions During Experiment

The release was made during the recovery phase of a principal magnetic storm that had occurred in the latter half of September 17, 1971. In the 24 hours preceding the storm, there had been a succession of magnetospheric substorms, the last, a minor one, occurring about 1:30 u.t. on September 21, 1971. The average planetary index K_p was 2 for the 3 hours prior to the release and 1 for the 3 hours following the release. On the whole, the magnetic field was relatively quiet during the experiment. Data from the HF auroral radar and the balloon-borne X-ray monitors indicated a low-intensity, though widespread, particle precipitation throughout the experiment. These data were entirely consistent with the structure of the ionospheric D-layer as deduced from riometer measurements and of the E- and F-layers as deduced from the ionosonde measurements. Data from ATS-5 satellite — located on approximately the same L-shell as the release, but displaced from it by about $25°$ to the east — indicated a low equatorial flux of 40-keV electrons. The relative magnetospheric quiescence reflected the inactivity of Sun as evidenced by the smallness of sunspot numbers, the absence of solar flares, the weak solar radio emissions, the moderate velocity and low proton fluxes associated with the solar wind.

Interaction Effects

There had been speculation in the literature (ref. 35) that the deposition of an ion cloud outside the plasmapause might induce an enhanced electron precipitation and thus produce an artificial aurora. Thus a sudden increase in the electron density resulting from the ion-cloud formation would be accompanied by an increase in the local refractive

index, and thus a lowering of the propagation velocity of the electron-cyclotron waves (whistlers). This decrease might reach the point at which resonance interaction with the energetic-electron component of the ambient medium might be expected. Theoretical studies of such interaction phenomena (ref. 36) indicated that if there is a sufficiently large anisotropy in pitch-angle distribution of the electrons, the resonant interaction would result in a conversion of the energy associated with the transverse component of the motion into energy of longitudinal motion. Hence, the electron velocity would become more nearly alined along the magnetic field lines, leading thereby to enhanced precipitation. The strength of such effects requires that the ambient cold-plasma density be sufficiently low so that the cloud deposition produces a significant perturbation and also that the energetic-electron flux be sufficiently large so as to provide an adequately strong interaction with the very low frequency (VLF) waves. At the time of the experiment, cloudy skies at Great Whale prohibited visual observations from there. However, no ionospheric or magnetic disturbances, which would have been expected to accompany enhanced precipitation, were detected. The low level of energetic-electron flux measured on ATS-5 has already been mentioned. Moreover, on the basis of the electric-field measurement (as described in the subsection entitled "Comparison With Magnetospheric Convection Models"), it appears that the release may well have taken place, if not interior to, at least bordering on the plasmasphere and that the ambient thermal electron density may therefore have been quite high. Based on the earlier considerations, a relatively weak interaction, at most, would have been expected. This, coupled with the fact that (from the magnetic-field data) the extremity of the field line at 100-km altitude was over 200 km from Great Whale, renders the absence of any artificial aurora hardly surprising.

There is, however, evidence of interaction phenomena of a related kind. The apparent energization of the ion cloud as manifested in the increase of the rate of cloud elongation during the first 300 seconds has already been noted (fig. 9(b)). With some plausibility, it can be argued that this arises through the resonant cyclotron interaction between the barium ions and the ELF waves. The gyration period of barium ions in the magnetic field in the proximity of the release was about a minute. Extremely low frequency waves having this periodicity are known to exist and indeed manifest themselves at ground level as magnetic micropulsations. They are believed to arise through magnetospheric cavity resonances (ref. 37). If through formative processes there was initially a sufficient anisotropy in the barium-ion pitch-angle distribution, a similar interaction to the one discussed previously between electrons and VLF waves might be expected Through such interaction, energy would be expected to be siphoned from the transverse into the longitudinal mode, thus leading to the higher rate of elongation. The interaction would diminish as isotropy was approached, and this would explain the quenching of the instability after 300 seconds.

CONCLUDING REMARKS

The NASA-Max Planck Institute Barium Ion Cloud (BIC) Experiment on September 21, 1971, established the usefulness of barium-ion-cloud releases as a magnetospheric research technique. Some of the more interesting conclusions derived from the experiment follow.

Electric Field

The more tenuous outermost striations rapidly acquired the velocity of the ambient thermal plasma. The subsequent drift, referred to an inertial frame, had an inward meridional component of 0.995 km/sec and an easterly azimuthal component of 3.62 km/sec. This drift is more nearly azimuthal than predicted on the basis of various proposed magnetospheric convective models and seemingly indicates little energization of the plasma in the proximity of the release. The fact that the plasma is drifting predominantly in the azimuthal direction suggests that the release at $L = 7.1$ was close to the boundary of the plasmasphere (L is the geocentric distance of field-line/equatorial-plane intercept in Earth radii). This appears at variance with the results of whistler measurements, which placed the plasmapause at an L-value of 4 to 4.5, though there was evidence of some irregular plasmaspheric structure out to larger L-values. There was, however, qualitative agreement with the whistler measurements in that the radially inward drift of the whistler ducts was observed at the time of the experiment.

The electric-field components deduced from the BIC plasma drifts were 0.19 mV/m in the westerly direction and 0.68 mV/m in the inward direction, referred to an inertial frame. These values are almost diametrically opposed to the estimates of the ionospheric electric fields from the balloon-borne instruments and the ground-based magnetometer data. These differences imply the existence of potential gradients along the magnetic field lines. The existence of such magnetic field-alined electric fields raises questions concerning the validity of the practice of relating the ionospheric and magnetospheric electric fields by assuming the magnetic field lines to be equipotentials.

Magnetic Field

The actual orientation of the magnetic field line through the release point as delineated by the ion cloud differed by about 10.5° from that predicted by a magnetic-field model which incorporated currents within the neutral sheet and the magnetopause. An equatorial ring current of 3.5 MA distributed between 5 and 8.5 Earth radii when added to the magnetic-field model provides agreement with observation. The unexpectedly large disparity reveals the need to incorporate the effects of ring current into magnetic-field models, if they are to provide a reasonably realistic representation of the magnetic field at distances of several Earth radii.

Formation of Striations and Deceleration of Cloud

Considerable striational structure was observed in the BIC release. These striational filaments formed during the transient phase of the cloud expansion through what is believed to have been a Rayleigh-Taylor instability at the expanding ion-cloud boundary. A time lag was noted between the formation of the striations and their breakaway from the main core. This anomalous behavior was attributed to their entrainment within the polarization wake of the main core. The existence of such a wake also explains why the main core decelerated more rapidly than had been theoretically predicted. Thus, some of its momentum would be imparted to the ambient plasma within the wake and, in addition, the presence of the wake would increase the area of interaction and, hence, resistive dissipation at ionospheric levels.

Other Interaction Effects

It was thought prior to the experiment that the increase in electron density resulting from the formation of the ion cloud might result in the slowing down of very low frequency waves, permitting a greater cyclotron interaction with the energetic electrons populating the magnetosphere and thus inducing an artificial aurora. Although the existence of cloudy skies at the Great Whale Geophysical Observatory near the foot of the field line precluded visual observations, no ionospheric or magnetic perturbations which might have been expected to accompany the increased electron precipitation were detected. There is evidence of interaction phenomena of a related kind. The observed increase in the rate of elongation of the ion cloud during the first 5 minutes may have resulted from the resonant cyclotron instability between the barium ions and extremely low frequency waves propagating through the magnetosphere.

Langley Research Center,
National Aeronautics and Space Administration,
Hampton, Va., January 22, 1975.

REFERENCES

1. Haerendel, G.; and Lüst, R.: Electric Fields in the Ionosphere and Magnetosphere. Particles and Fields in the Magnetosphere, B. M. McCormac, ed., Reidel Pub. Co. (Holland), 1971, pp. 213-218.

2. Adamson, David; and Fricke, Clifford L.: Barium Cloud Evolution and Striation Formation in the Magnetospheric Release on September 21, 1971. NASA TN D-7722, 1974.

3. Symposium on the NASA-MPE Barium Cloud Experiment. Trans., American Geophys. Union, vol. 53, no. 4, Apr. 1972, pp. 482-484.

4. Brence, W. A.; Carr, R. E.; Gerlach, J. C.; and Neuss, Hans: NASA/Max Planck Institute Barium Ion Cloud Project. J. Geophys. Res., vol. 78, no. 25, Sept. 1, 1973, pp. 5726-5731.

5. Davis, T. N.; Stanley, G. M.; and Boyd, J. S.: Geophysical Disturbance Environment During the NASA/MPE Barium Release at 5 R_E on September 21, 1971. J. Geophys. Res., vol. 78, no. 25, Sept. 1, 1973, pp. 5732-5735.

6. Mozer, F. S.; and Carpenter, D. L.: Balloon and VLF Whistler Measurements of Electric Fields, Equatorial Electron Density, and Precipitating Particles During a Barium Cloud Release in the Magnetosphere. J. Geophys. Res., vol. 78, no. 25, Sept. 1, 1973, pp. 5736-5744.

7. Manring, E. R.; and Patty, R. R.: Yield and Ion Distribution for the Barium Cloud at 31,000 Kilometers, September 21, 1971. J. Geophys. Res., vol. 78, no. 25, Sept. 1, 1973, pp. 5745-5750.

8. Mende, S. B.: Morphology of the Magnetospheric Barium Release. J. Geophys. Res., vol. 78, no. 25, Sept. 1, 1973, pp. 5751-5767.

9. Adamson, D.; Fricke, C. L.; Long, S. A. T.; Landon, W. F.; and Ridge, D. L.: Preliminary Analysis of NASA Optical Data Obtained in Barium Ion Cloud Experiment of September 21, 1971. J. Geophys. Res., vol. 78, no. 25, Sept. 1, 1973, pp. 5769-5784.

10. Hohl, Frank: Expansion of an Ion Cloud in the Earth's Magnetosphere. J. Geophys. Res., vol. 78, no. 25, Sept. 1, 1973, pp. 5785-5794.

11. Barish, Franklin D.; and Roederer, Juan G.: Experimental Test of Magnetospheric Models. J. Geophys. Res., vol. 78, no. 25, Sept. 1, 1973, pp. 5795-5801.

12. Axford, W. I.; and Hines, C. O.: A Unifying Theory of High-Latitude Geophysical Phenomena and Geomagnetic Storms. Canadian J. Phys., vol. 39, no. 10, Oct. 1961, pp. 1443-1464.

13. Dungey, J. W.: Interplanetary Magnetic Field and the Auroral Zones. Phys. Rev. Lett., vol. 6, no. 2, Jan. 15, 1961, pp. 47-48.

14. Frank, L. A.: Plasma in the Earth's Polar Magnetosphere. J. Geophys. Res., vol. 76, no. 22, Aug. 1, 1971, pp. 5202-5219.

15. Axford, W. I.; Petschek, H. E.; and Siscoe, G. L.: Tail of the Magnetosphere. J. Geophys. Res., vol. 70, no. 5, Mar. 1, 1965, pp. 1231-1236.

16. Long, Sheila Ann T.: Analytical Expressions for Position Error in Triangulation Solution of Point in Space for Several Station Configurations. NASA TN D-7552, 1974.

17. Long, Sheila Ann Thibeault: Triangulation Error Analysis for the Barium Ion Cloud Experiment. M.S. Thesis, North Carolina State Univ., 1973.

18. Long, Sheila Ann T.: Effects of Various Experimental Parameters on Errors in Triangulation Solution of Elongated Object in Space. NASA TN D-7802, 1975.

19. Knecht, David J.: The Geomagnetic Field (A Revision of Chapter 11, Handbook of Geophysics and Space Environments). AFCRL-72-0570, U.S. Air Force, Sept. 26, 1972. (Available from DDC as AD 759 837.)

20. Davidson, Robert E.: Ring Structure of a Neutral Gas Cloud Studied in a One-Dimensional Expansion Into Space. NASA TN D-6760, 1972.

21. Harp, Bill F.: Photogrammetric Calibration of the NASA-Wallops Island Image Intensifier System. Contract No. NAS 6-2066, DBA Systems, Inc., May 15, 1972. (Available as NASA CR-137455.)

22. Brown, Duane C.: A Treatment of Analytical Photogrammetry. AFMTC-TR-57-22, U.S. Air Force, Aug. 1957. (Available from DDC as AD 124 144.)

23. Brown, Duane C.: An Advanced Reduction and Calibration for Photogrammetric Cameras. AFCRL-64-40, U.S. Air Force, Jan. 1964. (Available from DDC as AD 431 886.)

24. Fricke, Clifford L.: Triangulation of Multistation Camera Data to Locate a Curved Line in Space. NASA TN D-7538, May 1974.

25. Cain, Joseph C.; Hendricks, Shirley J.; Langel, Robert A.; and Hudson, William V.: A Proposed Model for the International Geomagnetic Reference Field-1965. J. Geomagn. & Geoelec., vol. 19, no. 4, 1967, pp. 335-355.

26. Mead, Gilbert D.: Deformation of the Geomagnetic Field by the Solar Wind. J. Geophys. Res., vol. 69, no. 7, Apr. 1, 1964, pp. 1181-1195.

27. Williams, Donald J.; and Mead, Gilbert D.: Nightside Magnetosphere Configuration as Obtained From Trapped Electrons at 1100 Kilometers. J. Geophys. Res., vol. 70, no. 13, July 1, 1965, pp. 3017-3029.

28. Bostick, Winston H.: Experimental Study of Ionized Matter Projected Across a Magnetic Field. Phys. Rev., Second ser., vol. 104, no. 2, Oct. 15, 1956, pp. 292-299.

29. Schmidt, George: Plasma Motion Across Magnetic Fields. Phys. Fluids, vol. 3, no. 6, Nov.-Dec., 1960, pp. 961-965.

30. Scholer, Manfred: On the Motion of Artificial Ion Clouds in the Magnetosphere. Planetary & Space Sci., vol. 18, no. 7, July 1970, pp. 977-1004.

31. Longmire, Conrad L.: Elementary Plasma Physics. Interscience Publ., 1963, pp. 74-78.

32. Wolf, R. A.: Effects of Ionospheric Conductivity on Convective Flow of Plasma in the Magnetosphere. J. Geophys. Res., vol. 75, no. 25, Sept. 1, 1970, pp. 4677-4698.

33. Taylor, Harold E.; and Hones, Edward W., Jr.: Adiabatic Motion of Auroral Particles in a Model of the Electric and Magnetic Fields Surrounding the Earth. J. Geophys. Res., vol. 70, no. 15, Aug. 1, 1965, pp. 3605-3628.

34. Brice, Neil M.: Bulk Motion of the Magnetosphere. J. Geophys. Res., vol. 72, no. 21, Nov. 1, 1967, pp. 5193-5211.

35. Brice, Neil: Artificial Enhancement of Energetic Particle Precipitation Through Cold Plasma Injection: A Technique for Seeding Substorms? J. Geophys. Res., vol. 75, no. 25, Sept. 1, 1970, pp. 4890-4892.

36. Kennel, C. F.; and Petschek, H. E.: Limit on Stably Trapped Particle Fluxes. J. Geophys. Res., vol. 71, no. 1, Jan. 1, 1966, pp. 1-28.

37. McClay, J. F.: On the Resonant Modes of a Cavity and the Dynamical Properties of Micropulsations. Planetary & Space Sci., vol. 18, no. 12, Dec. 1970, pp. 1673-1690.